

Article

Open Access



Band convergence and defect engineering synergistically revamping the carrier-phonon dynamics in $\text{Mg}_{3-x}\text{Zn}_x\text{Sb}_2$ solid solutions: an experimental and theoretical insights

Priyadharshini Shanmugasundaram^{1,2}, Vijay Vaiyapuri^{1,3}, Kamalakannan Shanmugasundaram², Archana Jayaram¹, Hiroya Ikeda^{4,*}, Navaneethan Mani^{1,3,*}

¹Centre of Excellence in Materials for Advanced Technologies (CeMAT), Faculty of Engineering and Technology, SRM Institute of Science and Technology, Kattankulathur-603 203, India.

²Department of Physics and Nanotechnology, SRM Institute of Science and Technology, Kattankulathur-603 203, India.

³Nanotechnology Research Centre, Faculty of Engineering and Technology, SRM Institute of Science and Technology, Kattankulathur-603 203, India.

⁴Research Institute of Electronics, Shizuoka University, Shizuoka 432-8011, Japan.

*Correspondence to: Prof. Navaneethan Mani, Nanotechnology Research Centre, Faculty of Engineering and Technology, SRM Institute of Science and Technology, Kattankulathur-603 203, India. E-mail: navaneem@srmist.edu.in; Prof. Hiroya Ikeda, Research Institute of Electronics, Shizuoka University, 3-5-1 Johoku, Naka-ku, Hamamatsu, Shizuoka 432-8011, Japan. E-mail: ikeda.hiroya@shizuoka.ac.jp

How to cite this article: Shanmugasundaram, P.; Vaiyapuri, V.; Shanmugasundaram, K.; Jayaram, A.; Ikeda, H.; Mani, N. Band convergence and defect engineering synergistically revamping the carrier-phonon dynamics in $\text{Mg}_{3-x}\text{Zn}_x\text{Sb}_2$ solid solutions: an experimental and theoretical insights. *Energy Mater.* **2025**, *5*, 500100. <https://dx.doi.org/10.20517/energymater.2024.304>

Received: 26 Dec 2024 **First Decision:** 7 Feb 2025 **Revised:** 28 Feb 2025 **Accepted:** 13 Mar 2025 **Published:** 13 May 2025

Academic Editor: Yuping Wu **Copy Editor:** Ping Zhang **Production Editor:** Ping Zhang

Abstract

Mg_3Sb_2 -based n-type Zintl compounds have attracted greater attention for their superior thermoelectric performance, making them a potential candidate for medium-temperature (< 900 K) applications. Herein, this work verifies the p-type $\text{Mg}_{1.8}\text{Zn}_{1.2}\text{Sb}_2$ solid-solution and defect engineering could be the key mechanism to reduce the lattice thermal conductivity (κ_l) for improving the thermoelectric performance. The carrier and phonon transport properties were studied by adding heavy element Ag at Mg-sites of $\text{Mg}_{1.8}\text{Zn}_{1.2}\text{Sb}_2$ solid-solution. As a result, the $\text{Ag}_{0.03}\text{Mg}_{1.77}\text{Zn}_{1.2}\text{Sb}_2$ sample simultaneously obtained the maximum power factor of $456 \mu\text{W}/\text{mK}^2$ via band convergence and defect engineering, which led to reduced thermal conductivity of $0.56 \text{ W}/\text{mK}$ at 753 K by the strengthening of multiscale phonon scattering. In addition, optimized carrier density and thermal conductivity resulting in a maximum figure of merit (zT) of 0.5 at 753 K has been obtained for $\text{Ag}_{0.03}\text{Mg}_{1.77}\text{Zn}_{1.2}\text{Sb}_2$, which is 285% higher than undoped $\text{Mg}_{1.8}\text{Zn}_{1.2}\text{Sb}_2$. This work demonstrates that heavy element substitution induces band



© The Author(s) 2025. **Open Access** This article is licensed under a Creative Commons Attribution 4.0 International License (<https://creativecommons.org/licenses/by/4.0/>), which permits unrestricted use, sharing, adaptation, distribution and reproduction in any medium or format, for any purpose, even commercially, as long as you give appropriate credit to the original author(s) and the source, provide a link to the Creative Commons license, and indicate if changes were made.



convergence and that defect engineering leads to simultaneous improvement in thermoelectric transport properties of *p*-type $\text{Mg}_{1.8}\text{Zn}_{1.2}\text{Sb}_2$.

Keywords: $\text{Mg}_{1.8}\text{Zn}_{1.2}\text{Sb}_2$, defect engineering, solid solution, band convergence, thermal conductivity

INTRODUCTION

Thermoelectric (TE) materials have been significantly developed for heating and cooling applications. In this, the thermal energy is directly converted into electrical energy and vice versa by TE devices^[1,2]. Heat-to-energy conversion requires low lattice thermal conductivity (κ_L) and balancing charge mobility/carrier density (n) in crystalline solids. A dimensionless figure of merit (zT) represents the performance of TE devices,

$$zT = \frac{S^2\sigma}{(\kappa_B + \kappa_e + \kappa_L)}T \quad (1)$$

where S , σ , T , κ_B , and κ_e are denoted as the Seebeck coefficient, electrical conductivity, temperature, bipolar and electronic thermal conductivity, respectively^[3,4]. Also, the zT values will be varied according to multiple physical factors such as transport characteristics of carrier and phonon transport incorporated with the materials quality factor, ($\beta \propto \frac{\mu_w}{\kappa_L}$), which is linked to the weighted mobility (μ_w), and κ_L , respectively. Higher zT values should be required to improve the conversion efficiency of the devices. Therefore, some strategies were used to enhance the $S^2\sigma$ via band engineering such as band convergence^[5], band sharpening^[6], and energy filtering effect^[7]. Simultaneously, the thermal conductivity is reduced through defect engineering^[8], nanostructuring^[9], microstructural defects^[10], and suppression of the bipolar effect^[11].

Over the past decades, the following high-performance TE materials have been reported such as Bi_2Te_3 ^[12], PbTe ^[13], SnTe ^[14], GeTe ^[15], CoSb_3 ^[16], SnSe ^[17], AgSbTe_2 ^[18], and Zintl phase compounds^[19]. In this series, traditional Bi_2Te_3 -based TE materials have been well-known commercial and excellent room-temperature TE materials for low-grade heat recovery due to their high zT . However, it contains a toxic and high-cost element of tellurium and poor mechanical strength which limits its further development and usage in real-time TE applications. A few disadvantages result from the strongly anisotropic transport properties because the layered crystal structure exhibits weak Van der Waals bonds. In addition, the presence of Te in Bi_2Te_3 -based devices restricts its usage and makes it unstable above 500 K. In search of alternative materials for low-grade heat recovery, TE materials should satisfy the conditions including being inexpensive, non-toxic, and highly efficient performance for the next-generation modules. Zintl-based compounds have gained considerable attention for TE applications due to their complex crystal structures and the use of earth-abundant and inexpensive elements with decent TE performance^[20].

Mg_3X_2 ($x = \text{Bi/Sb}$) intermetallic compounds were introduced by Zintl and Husemann in the year 1930 and are defined as Zintl phase compounds. Recently, Zintl phase compounds have been well-recognized as a potential and proficient material for room-to-mid-temperature TE applications due to their excellent performance and cost-effectiveness. In addition, Zintl materials have been potential candidates for various applications such as batteries^[21], photovoltaics^[22], catalysts^[23], hydrogen storage materials^[24], and so on. Especially, the TE performance of Mg_3Sb_2 has been improved by using doping with a mixture of iso and aliovalent alkali metals^[25]. This is an ideal representative of the phonon-glass and electron-crystal (PGEC) mechanism. In recent times, *p*-type AB_2X_2 -based Zintl has exhibited notable TE performance, in which “A” is the Eu, Ba, Ca, Mg, Yb, “B” is the Mg, Cd, Zn, Na, and “C” is the Sb/Bi^[26,27]. Compared with aliovalent doping, dual/higher element doping plays a major role in enhancing the n /carrier mobility (μ) via band

engineering, and simultaneously reduces the κ_L by manipulation of defect engineering which will enhance the phonon scattering.

In common, both *n* and *p*-type semiconductor legs are more important for device fabrication purposes^[28]. The excellent performance of *n*-type Mg_3Sb_2 was realized, and its outcome shows a clear understanding of defect chemistry (Mg vacancies and Mg interstitials) and electron doping (Bi), which alters the physical and optical properties of the materials. Therefore, the room-temperature performance of $\text{Mg}_3\text{Sb}_{3-x}\text{Bi}_x$ -based materials shows a state-of-the-art *zT* and an alternative material for traditional Bi_2Te_3 -based materials^[29]. In the group of Zintl phase, *n*-type $\text{Mg}_3(\text{Sb}, \text{Bi})_2$ -based materials are known as promising and highly efficient materials with the benefits of cost-effectiveness and more stability. The Mg_3Sb_2 -based compounds exhibited a *p*-type semiconductor nature with a band gap of ~ 0.6 – 0.8 eV. In contrast, Mg_3Bi_2 is metallic in nature, but the introduction of excess Mg leads to semiconducting behavior^[30]. According to earlier reports, a high *zT* of 1.51 at 773 K was achieved by the introduction of excess Mg for *n*- $\text{Mg}_{3.2}\text{Sb}_{1.5}\text{Bi}_{0.49}\text{Te}_{0.01}$. Similarly, the excellent TE performance of *n*-type Mg_3Sb_2 with hierarchical microstructure and band degeneracy strategies achieved an extraordinary *zT* of 1.85 at 723 K due to its complex crystal structure and high valley degeneracy ($N_v = 6$)^[31,32]. Jiang *et al.* demonstrated a conversion efficiency of 10.6% for *n*-type Mg_3Sb_2 -based devices^[33].

At the same time, the *p*-type Mg_3Sb_2 achieves a low *zT* < 1 , which is lower than its *n*-type counterpart because of its low electrical transport properties (minimal *n* and μ) with the low valence band (VB) degeneracy ($N_v = 1$). Its strong chemical bonding enhances κ_L ^[34]. According to Li *et al.*, *p*-type Mg_3Sb_2 with double substitution achieved a peak *zT* of ~ 1.0 at 773 K via alloy scattering^[35]. Also, simultaneous modification of cationic and anionic sites of *p*-type Mg_3Sb_2 achieves the highest peak *zT* of 0.85 at 723 K^[36]. Furthermore, the conversion efficiency of 5.5% was obtained with uni-couple *p*-type $\text{Mg}_{1.594}\text{Yb}_{0.2}\text{Na}_{0.006}\text{Zn}_{1.2}\text{Sb}_2$ and *n*-type $\text{Mg}_{3.2}\text{SbBi}_{0.99}\text{Te}_{0.01}$ ^[37]. However, its low conversion efficiency prohibits the implementation of *p*-type Mg_3Sb_2 -based TE devices. Therefore, regulating the electrical transport properties of *p*-type Mg_3Sb_2 is essential for improving the peak *zT* and conversion efficiency of the TE device^[38].

According to recent research, Zn doping at Mg sites increases the σ via band convergence^[39,40]. To be specific, the superior TE performance of $\text{Mg}_{1.8}\text{Zn}_{1.2}\text{Sb}_2$ solid solutions has grabbed the curiosity of researchers. The $\text{Mg}_{1.8}\text{Zn}_{1.2}\text{Sb}_2$ framework has been widely studied compared to Mg_3Sb_2 , which possesses an anti- La_2O_3 structure (space group - $\text{P}\bar{3}\text{m1}$). The Zn atom occupies up to 67% of the tetrahedra in the $\text{Mg}_{3-x}\text{Zn}_x\text{Sb}_2$ structure, maintaining an identical atomic arrangement. It is widely acknowledged that zinc is preferred to fill the tetrahedral voids compared to octahedral ones. This might be due to the sp^3 orbitals rather than the localized d-ones which are essentially accountable for forming bonds. This structural approach reveals that, when disregarding symmetry changes, the structure of $\text{Mg}_{3-x}\text{Zn}_x\text{Sb}_2$ is remarkably different from the frameworks of other substituted Mg_3Sb_2 -based phases as XMg_2Sb_2 (where X is Ba/Ca/Sr). The Coulombic repulsion was diminished throughout the Mg_3Sb_2 system through the introduction of Zn, which produced a significantly less distance among Sb atoms and fewer positive charges. Due to lesser electronegativity (1.65 vs. 1.31 for Mg) and smaller atomic radius (1.35 vs. 1.50 Å for Mg), ends up in a lesser positive charge on the Zn atoms, which fulfils both prerequisites. By modulating the band structure of *p*-type Mg_3Sb_2 , Zn introduction at the Mg site may improve its electrical performance; however, Zn excess will lead to a narrow band gap. Thus, this work aims to provide a tellurium-free, cost-effective, and one-step synthesis of Mg_3Sb_2 -based solid solution for room-to-mid-temperature TE applications.

To elucidate the band and defect engineering in *p*-type $\text{Mg}_{1.8}\text{Zn}_{1.2}\text{Sb}_2$, we performed experimental and theoretical studies of undoped and Ag-doped *p*-type $\text{Mg}_{1.8}\text{Zn}_{1.2}\text{Sb}_2$ samples. The introduction of monovalent

Ag at Mg site significantly increases the n and σ of 225 S/cm at 303 K. Along with that, the VB convergence increases the S of 257 $\mu\text{V/K}$ at 753 K. Simultaneously, phonon transport is enhanced through multiscale defect scatterings, which reduces the κ_L to 0.56 W/mK at 753 K for $\text{Ag}_{0.03}\text{Mg}_{1.77}\text{Zn}_{1.2}\text{Sb}_2$. This increment in carrier transport and strong phonon transport of $\text{Ag}_{0.03}\text{Mg}_{1.77}\text{Zn}_{1.2}\text{Sb}_2$ synergistically achieved a peak zT of 0.5 at 753 K, which is $\sim 285\%$ higher than undoped $\text{Mg}_{1.8}\text{Zn}_{1.2}\text{Sb}_2$. This study suggests that the heavy/aliovalent substitution on the $\text{Mg}_{1.8}\text{Zn}_{1.2}\text{Sb}_2$ system simultaneously optimizes the carrier and phonon transport, which helps to develop a potential candidate for room-to-mid-temperature TE applications.

EXPERIMENTAL

Materials preparation of p-type $\text{Mg}_{1.8}\text{Zn}_{1.2}\text{Sb}_2$ and $\text{Ag}_x\text{Mg}_{1.8-x}\text{Zn}_{1.2}\text{Sb}_2$ pellets

The p-type $\text{Mg}_{1.8}\text{Zn}_{1.2}\text{Sb}_2$ and $\text{Ag}_x\text{Mg}_{1.8-x}\text{Zn}_{1.2}\text{Sb}_2$ ($x = 0, 0.01, 0.03$, and 0.05) samples were prepared by a spark plasma sintering technique. Magnesium (Mg, 99.5%, metal turnings), zinc (Zn, 99.5%, metal powder), silver (Ag, 98.8%, metal powder), and antimony (Sb, 99.5%, metal powder) were weighed according to the stoichiometric ratio of $\text{Ag}_x\text{Mg}_{1.8-x}\text{Zn}_{1.2}\text{Sb}_2$ ($x = 0, 0.01, 0.03$ and 0.05). All elements of Mg, Sb, Ag, and Zn metal powders were grounded using mortar and pestle. The grounded powders were loaded into a cylindrical graphite die (inner diameter 13 mm) and subjected to sintering via spark plasma sintering technique at 873 K under the pressure of 40 MPa for 5 min holding time and cooling rate (50 $^\circ\text{C/min}$) to obtain dense disk-shaped pellets [Supplementary Scheme 1A and B].

Structural characterizations and TE transport property measurements

X-ray diffraction (XRD) was used for the phase composition of each sample characterized by the help of a PANalytical multipurpose diffractometer under $\text{CuK}\alpha$ radiation ($\lambda = 1.5406 \text{ \AA}$). High-resolution transmission electron microscopy (HR-TEM; JEOL JEM-2100 Plus with an operating voltage of 200 kV). The microstructure and compositional analysis of the samples was performed using high-resolution scanning electron microscopy (HR-SEM; Thermoscientific ApreoS) equipped with energy dispersive spectroscopy (EDS). Thermal conductivity (κ) was calculated by $\kappa = \rho DC_p$, where ρ is the sample density (estimated based on the Archimedes method), D is the thermal diffusivity (measured by a laser flash apparatus (LFA 467 HT, NETZSCH)), and C_p is the specific heat (determined by differential scanning calorimetry thermal analyzer). The σ and S were simultaneously measured by a commercial ADVANCE RIKO ZEM-3 system under a helium atmosphere. The room temperature Hall measurement was measured by using ECOPIA HMS 5300. The sample's carrier concentration (n) and mobility (μ) were calculated using the four-probe Van der Pauw method under a magnetic field.

Computational methods

All the periodic density functional calculations were computed by using the Vienna Ab initio Simulation Package (VASP), with the Projected Augmented Wave (PAW) method applied to account for the electron-ion interaction terms. The VASP package utilizes the Perdew-Burke Ernzerhof (PBE) exchange-correlation function in combination with PAW potentials. The convergence criteria of 0.03 eV/ \AA in force and 10^{-5} eV in energy were adopted to optimize the supercells. The Monkhorst-Pack K-point mesh calculated the relaxation and self-consistent computations of the crystal structures^[41]. In general, the exchange-correlation energy comprises the exchange energy (from the Pauli exclusion principle) and the correlation energy (from Coulomb interaction effects), which are treated in terms of different approximations, expressed as $E_{\text{total}}[\rho] = T_s[\rho] + E_{\text{ext}}[\rho] + E_H[\rho] + E_{\text{xc}}[\rho]$, where $T_s[\rho]$ is kinetic energy (KE) of non-interacting electrons, $E_{\text{ext}}[\rho]$ is external potential energy (PE), $E_H[\rho]$ is classical Hartree energy, and $E_{\text{xc}}[\rho]$ is exchange-correlation energy. In our work, the Monkhorst-Pack grid generates a uniform K-point grid of $3 \times 3 \times 2$ for geometry optimization and $6 \times 6 \times 4$ for electronic structure simulations. In addition, the basis set is a critical factor that directly determines the accuracy and efficiency of electronic structure prediction and is mainly based on the (I) plane wave basis set and (II) pseudopotentials. The formation

energy (ΔE_{form}) of the Zn and Ag at Mg_3Sb_2 is calculated by $\Delta E_{\text{form}}(\text{ZnAg-Mg}_3\text{Sb}_2) = E_{(\text{ZnAg-Mg}_3\text{Sb}_2)} - (E_{\text{Zn-Mg}_3\text{Sb}_2} + E_{\text{Ag}})$, where $\text{Zn-Ag-Mg}_3\text{Sb}_2$, $E_{(\text{ZnAg-Mg}_3\text{Sb}_2)}$, and E_{Ag} denote the total energy of the Zn-Ag doped Mg_3Sb_2 system, the total energy of $\text{Zn@Mg}_3\text{Sb}_2$ without Ag dopant, and the total energies of Ag in the bulk phase, respectively. A plane-wave basis with a cutoff of 900 eV was used to calculate electron densities and wave functions. Electronic structure calculations, i.e., total density of states (TDOS), projected density of states (PDOS), band structure, and electron density analysis, were then simulated using the most stable geometries. All optimized structures presented in this study were taken from the VESTA packages.

RESULTS AND DISCUSSIONS

Schematic illustration of the crystal structures and XRD of $\text{Ag}_x\text{Mg}_{1.8-x}\text{Zn}_{1.2}\text{Sb}_2$

The $\text{Mg}_{1.8}\text{Zn}_{1.2}\text{Sb}_2$ samples expose the hexagonal crystal structures with a space group of $p\bar{3}m1$. Zn is the suitable acceptor for boosting the density of holes, as well as enhancing the electronic transport properties, resulting in a narrow bandgap and manipulating the band structure in the Mg_3Sb_2 system. There are two distinct crystallographic sites of Mg atoms available in Mg_3Sb_2 : $\text{Mg}^{2+}/(\text{Mg1-octahedral})$ and $[\text{Mg}_2\text{Sb}_2]^{2-}/(\text{Mg2-tetrahedral})$. The Zn atoms are potential substitution for tetrahedral sites and proximity to neighbouring Sb atoms assists in an overall decrease in coulombic repulsion. Specifically, zinc atoms have lower electronegativity ($\chi = 1.65$), shorter atomic radius (142 p.m.), and a smaller positive charge than magnesium atoms. The electronegativity difference ($\Delta\chi$) between the substitution (Mg) and foreign atom (Zn) was a more important parameter to enhance the transport properties and produced internal defects. In general, the $\Delta\chi$ was calculated by $|\Delta\chi| = |\chi_{\text{Host}} - \chi_{\text{dopant}}|$. The calculated $\Delta\chi$ between Zn at the Mg site is 0.29 and at the Sb site is 0.12 [Supplementary Table 1]. In addition, the smaller positive charges of Zn atoms are substituted at Mg sites to enhance the transport properties of Mg_3Sb_2 . The differences in electronegativity and atomic mass with host and dopant sites are shown in Supplementary Figure 1A and B. Additionally, this contains multiple states compared to Mg_3Sb_2 and is situated below the Fermi level (E_F) which manipulates its band structure through a band convergence strategy. For further enhancing the TE transport properties, the heavy and aliovalent element Ag was introduced at Mg sites of $\text{Mg}_{1.8}\text{Zn}_{1.2}\text{Sb}_2$.

Figure 1A and B illustrates the hexagonal crystal structure of undoped and Ag-substituted $\text{Mg}_{1.8}\text{Zn}_{1.2}\text{Sb}_2$. The XRD image of Ag-substituted $\text{Mg}_{1.8}\text{Zn}_{1.2}\text{Sb}_2$ ($x = 0, 0.01, 0.03$, and 0.05) samples were shown in Figure 1C. The introduction of Ag in $\text{Mg}_{1.8}\text{Zn}_{1.2}\text{Sb}_2$ shows a lower angle shift in the XRD result, where a secondary Sb phase was observed at 42.4° (JCPDS NO: 96-901-3011). As can be seen, the occurrence of Mg vacancies (V_{Mg}^{2-}) is due to the vaporization of Mg during heat treatment. The presence of secondary Sb can confirm the negative formation energy of low energy acceptor defect as V_{Mg}^{2-} at the lattice which act as acceptor defects ($Mg_{\text{Mg}} = V_{\text{Mg}}^{2-} + 2h$). These defects promote a greater number of holes or absorb excess electrons, and lead to the p -type pinning behavior through the introduction of energy states that are close to the VB^[42]. Here, the p -type materials pin the E_F , enabling the system in an equilibrium state via intrinsic acceptor defects and the material retains its p -type nature and reduces E_F (If n -type materials pin the E_F due to domination of intrinsic donor defects, the material remains n -type).

The ability to function as p -type TE semiconductors without any impurity substitution is caused by the formation of an adequate number of robust cation site vacancies^[43,44]. Figure 1D represents the expanded portion of XRD analysis, which confirms the lower angle shift leads to the expansion and tensile strain. In the Mg_3Sb_2 system, Zn has a large solubility limit (70%-90%) because of its (134 pm) minimal ionic radius compared with Mg (145 pm)^[45,46]. The increment of lattice parameters confirms the replacement of Mg^{2+} ions with Zn^{2+} and Ag^+ ions at the Mg sites, which decreases the crystallite size and indicates the contribution of strain in the lattice.

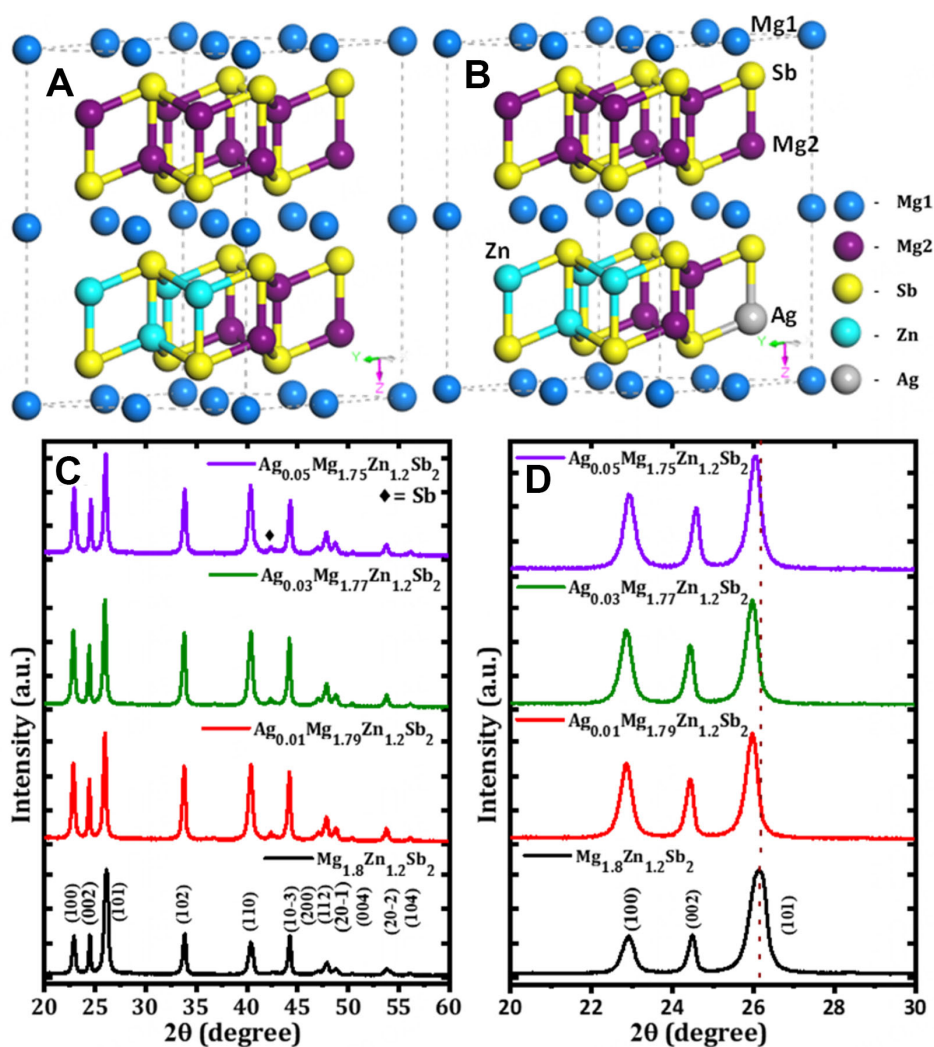


Figure 1. (A and B) crystal structures; (C and D) XRD and magnified XRD pattern of $\text{Ag}_x\text{Mg}_{1.8-x}\text{Zn}_{1.2}\text{Sb}_2$ ($x = 0, 0.01, 0.03$ and 0.05) samples. XRD: X-ray diffraction.

However, the observed trend with XRD peak shifts upon increasing Ag content in $\text{Mg}_{1.8}\text{Zn}_{1.2}\text{Sb}_2$ can be attributed to competing effects of lattice expansion and contraction. Initially, Ag-substituted samples show a lower angle shift for $x = 0.01$ and 0.03 samples, due to a higher atomic radius of Ag (165 pm) than that of Mg (145 pm)^[45]. It confirms the lattice expansion leading to tensile strain, resulting in increasing lattice parameters ($a = 4.484 \text{ \AA}$ to 4.508 \AA and $c = 7.232 \text{ \AA}$ to 7.259 \AA) and unit cell volume (125.97 \AA^3 to 127.08 \AA^3) [Supplementary Figure 1C and D]. After the Ag concentration exceeds $x > 0.03$, the peak shifted to a higher angle, due to the solubility limit, local structure distortions, and phase segregation, respectively^[47]. Beyond the solubility limit of Ag in $\text{Mg}_{1.8}\text{Zn}_{1.2}\text{Sb}_2$ system, the excess Ag occupies interstitial sites that expand the strain in the lattice. Also, this obtained trend of results were considered with the previously reported literatures^[48,49]. Furthermore, the microstructural properties and elemental distribution were analyzed by HR-SEM and EDS mapping [Supplementary Figure 2A-H]. Further, the EDS spectrum analysis and elemental compositions confirm the presence of Ag in the as-prepared compounds which is shown in Supplementary Figure 3A-D and Supplementary Table 2.

Carrier transport properties of $\text{Ag}_x\text{Mg}_{1.8-x}\text{Zn}_{1.2}\text{Sb}_2$

Figure 2A represents the schematic representation of the band diagram for undoped Mg_3Sb_2 , $\text{Mg}_{1.8}\text{Zn}_{1.2}\text{Sb}_2$, and Ag-doped $\text{Mg}_{1.8}\text{Zn}_{1.2}\text{Sb}_2$ systems, which confirms the role of the heavy element Ag in the lighter Mg site led to E_F towards the VB and enhanced hole concentration, which reduces the band gap. Figure 2B indicates the VB convergence before and after heavy element substitution in the $\text{Mg}_{1.8}\text{Zn}_{1.2}\text{Sb}_2$ matrix. This scheme represents that, Ag substitution leads to narrowed band gap and enhance the valley degeneracy, respectively. Figure 2C shows the room temperature Hall carrier density of $\text{Ag}_x\text{Mg}_{1.8-x}\text{Zn}_{1.2}\text{Sb}_2$ ($x = 0 - 0.05$). The n and μ could be explained by the relation,

$$n_H = \frac{1}{eR_H} \quad (2)$$

$$\mu_H = \sigma R_H \text{ or } \mu = \frac{e \langle \tau \rangle}{m^*} \quad (3)$$

Where e is the charge of an electron, and R_H is Hall coefficient. Here, positive n values indicate the domination of holes in the prepared system, which confirms that all the prepared samples exhibit a p -type semiconductor behavior at room temperature. $\text{Mg}_{1.8}\text{Zn}_{1.2}\text{Sb}_2$ shows a low hole n of $6.40 \times 10^{18} \text{ cm}^{-3}$; the introduction of Ag leads to an increase in the number of holes. This enhanced n confirms that Ag^+ substitution replaces the $[\text{Mg}_2\text{Sb}_2]^{2-}$ layers, which is an octahedral site of Mg_3Sb_2 with polar covalent bonding. Particularly, the $\text{Ag}_{0.05}\text{Mg}_{1.75}\text{Zn}_{1.2}\text{Sb}_2$ sample obtains the highest n of $8.19 \times 10^{19} \text{ cm}^{-3}$. In comparison with previous reports, Ag substitution at Mg sites increases the n , due to the convergence of bands producing excess holes near the VB and attaining a narrow band gap, which is confirmed by band structure calculation^[50]. Therefore, these results confirm that the foreign element (Ag) substitution enhances the domination of the ionized impurity scattering mechanism at 303 K^[51]. The introduction of Ag leads to improving the density of states (DOS) with band convergence, which increases the electrical transport properties via manipulation of the hole's concentration and enhances the material's TE performance. Figure 2D shows the Hall μ . In general, the μ can be expressed as Equation 3, where m^* is an effective mass of the electrons, and $\langle \tau \rangle$ is the average relaxation time. Here, relaxation time is a combination of m^* , temperature, and energy carriers, which is expressed as $\tau \propto E^r T^s (m^*)^t$. The highest μ of $145 \text{ cm}^2/\text{Vs}$ is obtained for the $\text{Ag}_{0.05}\text{Mg}_{1.75}\text{Zn}_{1.2}\text{Sb}_2$ at room temperature, which is 56% higher than the undoped sample. Specifically, the high μ weakens the polar covalent bonding and the carriers move faster than regular, due to the reduction of carrier scattering^[52]. It may arise via secondary impurities (Sb) and intrinsic Mg vacancies, which place interstitial sites between Mg and Sb. This weak polar covalent bonding in the $[\text{Mg}_2\text{Sb}_2]^{2-}$ layer helps to improve the $S^2\sigma$. Thus, the increasing trend of μ at 303 K confirms the Zn, and substitution of Ag confirms the domination of carrier scattering mechanism from a mixed scattering of ionized impurity and acoustic phonon scattering. Also, Ag at Mg sites softens the chemical bonds of the $\text{Mg}_{1.8}\text{Zn}_{1.2}\text{Sb}_2$ system^[34].

The σ was measured for $\text{Ag}_x\text{Mg}_{1.8-x}\text{Zn}_{1.2}\text{Sb}_2$ ($x = 0 - 0.05$) samples [Figure 3A]. In general, the σ of the material was estimated by $\sigma = ne\mu$, where e indicates electronic charge. For $\text{Mg}_{1.8}\text{Zn}_{1.2}\text{Sb}_2$, the σ increases from 77 S/cm to 157 S/cm at 303 K - 753 K, and the increasing trend of σ indicates the typical non-degenerate semiconductor behavior^[30]. Further, the σ of Ag-substituted $\text{Mg}_{1.8}\text{Zn}_{1.2}\text{Sb}_2$ increases, which confirming the aliovalent substitution enhances the hole concentration. Simultaneously, isovalent Zn increases μ via ionized impurity scattering^[40]. The σ values were improved after substituting Ag at Mg sites from 38 to 225 S/cm at room temperature, which was 193% greater than undoped $\text{Mg}_{1.8}\text{Zn}_{1.2}\text{Sb}_2$. To be specific, the $\text{Ag}_{0.05}\text{Mg}_{1.75}\text{Zn}_{1.2}\text{Sb}_2$ sample shows a drastic improvement in σ of 225 S/cm at 303 K due to a significant improvement of n and μ . However, when the temperature increased, the downward trend of σ indicates the typical heavily doped degenerate semiconductor behavior of Ag-substituted samples. Thus, the Ag atom could migrate to the $\text{Mg}_{1.8}\text{Zn}_{1.2}\text{Sb}_2$ lattice and take the sites of Mg atoms and interstitial sites, which

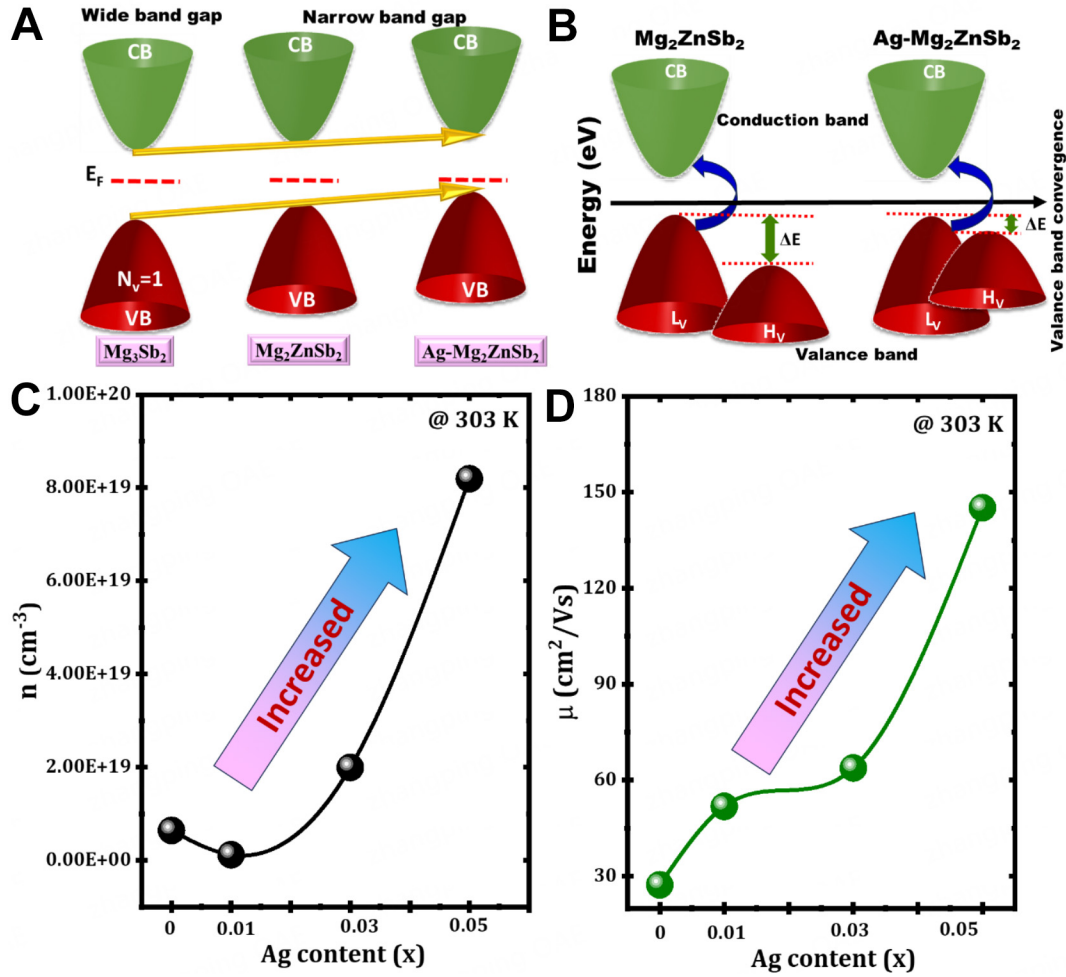


Figure 2. (A and B) schematic representation of band diagram (C) Hall carrier density, and (D) mobility of Ag_xMg_{1.8-x}Zn_{1.2}Sb₂ ($x = 0, 0.01, 0.03$, and 0.05) samples.

induces additional domination of minority carriers and secondary Sb at higher temperatures. This typical phenomenon resulting a reduction of σ via low hole concentration (i.e., hole trapping)^[53,54].

The obtained n and the measured S values are positive, indicating that holes are the majority carrier, and electrons are minority carriers in undoped and Ag-substituted Mg_{1.8}Zn_{1.2}Sb₂ samples, which are displayed in Figure 3B. In general, the S can be evaluated by the semiclassical Mott-Jones formula^[55]

$$S = \frac{8\pi^2 k_B^2}{3eh^2} m^* T \left(\frac{\pi}{3n} \right)^{\frac{2}{3}} \quad (4)$$

where k_B is Boltzmann constant, h is Plank constant, m_d^* is DOS carrier m^* , and e is an elemental charge. The S is directly proportional to m^* and indirectly proportional to the n . Here, compared with the undoped sample, the Ag_{0.05}Mg_{1.75}Zn_{1.2}Sb₂ sample attains a higher n of 8.19×10^{19} cm⁻³. $m_b^* = N_V^{2/3} m_d^*$, where N_V is the valley degeneracy and m_d^* is the average m^* of a single valley ($N_V = 1$), which can be used to calculate m_d^* . The S of Mg_{1.8}Zn_{1.2}Sb₂ is 234.7 μ V/K at 303 K, and 103 μ V/K at 753 K. After Ag substitution at Mg_{1.8}Zn_{1.2}Sb₂, the S trend was directly opposite to the undoped sample, which increases with temperature, indicating non-degenerate semiconductor behavior. Specifically, a convex-like trend of S indicates the influence of

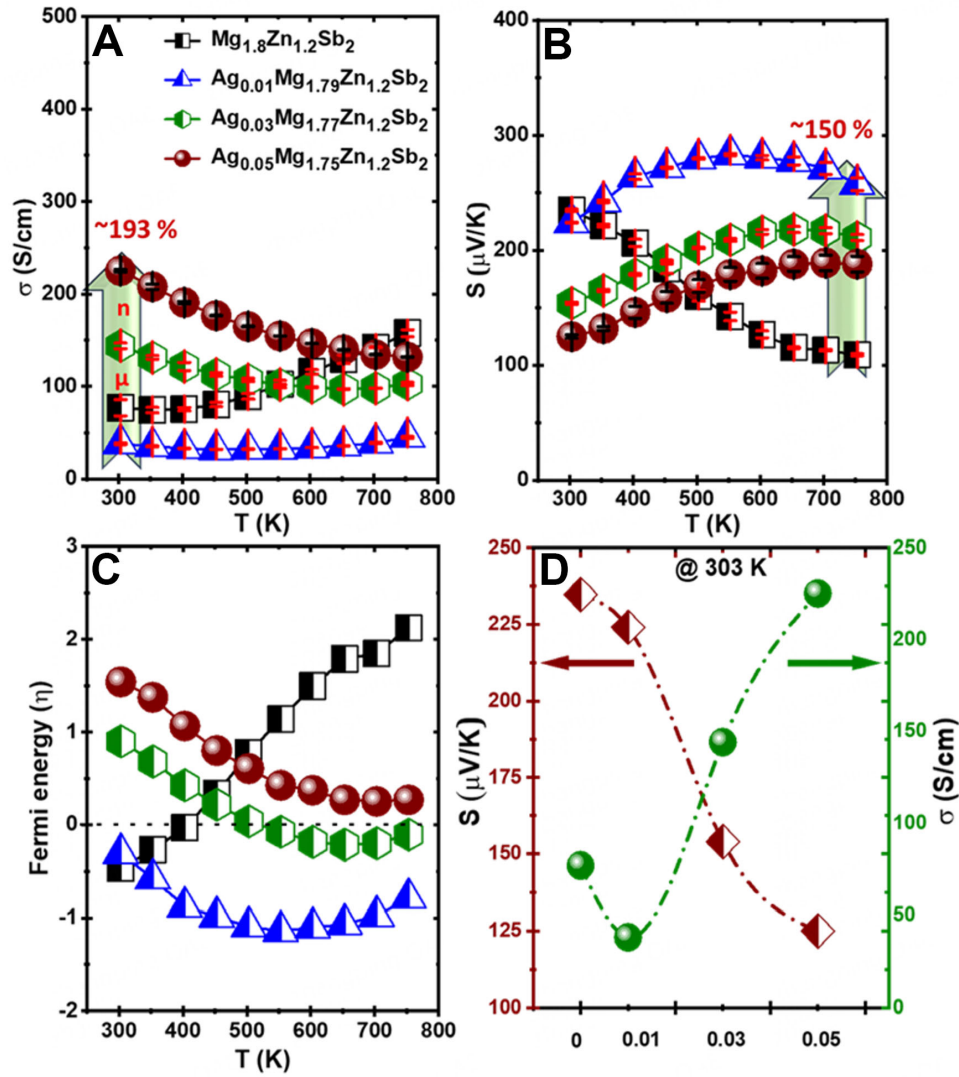


Figure 3. Temperature dependence of (A) electrical conductivity; (B) Seebeck coefficient; (C) Fermi energy; and (D) S vs. σ for $\text{Ag}_x\text{Mg}_{1.8-x}\text{Zn}_{1.2}\text{Sb}_2$ ($x = 0, 0.01, 0.03$ and 0.05) samples.

minority charge carriers, secondary Sb, and interstitial Ag atoms, which play a major role at high temperatures^[56]. Therefore, orbital overlap and the strengthening of chemical bond covalency and smaller electronegativity of Ag atom results in an enhanced DOS m^* via VB convergence, which helps to enhance the S at high temperatures. This finding emphasizes that, the bipolar diffusion effect is possible when VB electrons are thermally excited to the conduction band (CB) even at relatively lower temperatures^[57].

Consequently, the peak of S shifts to lower temperatures while the σ continuously increases with Ag concentration. Also, the $\text{Ag}_{0.01}\text{Mg}_{1.79}\text{Zn}_{1.2}\text{Sb}_2$ shows a drastic improvement in the S of 283 $\mu\text{V/K}$ at 553 K and 257 $\mu\text{V/K}$ at 753 K; it might be due to the enhancement of VB convergence, which exhibits a narrow band gap and lowers the energy separation. This increases the S at high temperatures by enhancing the electronic DOS and inhibiting bipolar conduction^[58]. Therefore, the introduction of VB convergence is a significant advantage in improving the S and TE performance over a broad temperature range. This indicates that, the interstitial silver (Ag) atoms, minority charge carriers, and secondary Sb have significant impacts at high

temperatures. Ag-substituted samples have a S approximately 150% higher than undoped $\text{Mg}_{1.8}\text{Zn}_{1.2}\text{Sb}_2$, due to hole excitation into heavier bands, enhancing VB convergence^[59]. Thus, this finding suggests that VB convergence adds a substantial benefit to the S and TE performance across a wide temperature range.

The contribution of impurity or secondary phase was confirmed by the reduced E_F ($\eta = E_F/k_B T$) using the S ($\sigma \times \exp\left[\frac{|S|}{k_B/e} - 2\right]$) and σ ($\ln\left[\exp\left(\frac{\sigma}{\sigma_{E_0}}\right) - 1\right]$) values, as shown in [Figure 3C](#). At room temperature, positive values indicated an increased hole concentration. At higher temperatures, negative values suggested the influence of minority charge carriers, highlighting the significant role of secondary Sb in contributing to bipolar conductivity. [Figure 3D](#) represents the σ and S vs. Ag content at 303 K, which confirms the typical semiconductor behavior of the as-prepared samples^[60].

Density functional theory representation of $\text{Ag}_x\text{Mg}_{1.8-x}\text{Zn}_{1.2}\text{Sb}_2$

The periodic density functional calculations were performed to gain insight on the TE properties of Mg_2ZnSb_2 compounds. The optimized geometries and formation energy of undoped, Zn, and Zn-Ag substituted Mg_3Sb_2 systems are shown in [Supplementary Figure 4A-E](#). Here, the computed band diagrams, PDOS plots, and electron density difference of Mg_2ZnSb_2 and Ag- Mg_2ZnSb_2 systems are provided in [Figure 4](#). The VB at the high symmetry point Γ and the CB at A indicate the indirect nature of the band explained in [Figure 4A](#)^[61]. The VB and CB of Mg_2ZnSb_2 and Ag- Mg_2ZnSb_2 systems are composed of the p -orbital of Sb and s -orbital of Mg, respectively. The obtained temperature-dependent S trend has been significantly changed after Ag doping due to the following phenomenon: VB convergence, which is highly consistent with the previous reports^[62,63]. It is a potential strategy, where the multiple VB maxima (VBM) (i.e., light and heavy VBs) of the material exist at nearly the same energy level which enhances the DOS near the E_F , resulting in enhanced S . On the other hand, the convergence of multi-band improves the mobility of holes and increases the σ . Therefore, the significant enhancement of S and σ enhances the overall power factor (PF) and TE performance. This VB convergence can be introduced via doping impurities, alloying, or strain engineering, respectively^[64]. The Mg_3Sb_2 intrinsically exhibits a wide band gap of ~ 0.6 – 0.8 eV and lower valley degeneracy ($N_v = 1$), which renders the TE performance^[65]. In this present investigation, the S of undoped $\text{Mg}_{1.8}\text{Zn}_{1.2}\text{Sb}_2$ sample decreased with temperature indicating the semiconductor behavior, whereas Ag-doped samples show an increasing trend with temperature due to the following reasons. Here, the substitution of isovalent Zn atom replaces $\sim 60\%$ Mg atoms and only settles in the tetrahedral $[\text{Mg}_2\text{Sb}_2]^{2-}$ sites, resulting in reducing the band gap from 0.28 eV (Mg_3Sb_2) to narrow the band gap of 0.16 eV ($\text{Mg}_{1.8}\text{Zn}_{1.2}\text{Sb}_2$) with increased valley degeneracy [[Supplementary Figure 5A](#)]^[63]. The DOS and PDOS for the Mg_3Sb_2 system explain the presence of Mg- s , Mg- p , Sb- s , and Sb- p orbitals, as shown in [Supplementary Figure 5B-D](#). Substituting the heavy element Ag^+ at anionic Mg_2 site of $\text{Mg}_{1.8}\text{Zn}_{1.2}\text{Sb}_2$ system introduces additional acceptor levels and exhibits the convergence of heavy VB Γ and lighter VB A near E_F of the band structure. The VB modification enhances the DOS and improves the TE performance of the Ag-substituted $\text{Mg}_{1.8}\text{Zn}_{1.2}\text{Sb}_2$ system^[45]. In addition, this phenomenon helps increase the DOS m^* of the system which significantly improves the S of $103 \mu\text{V/K}$ to $257 \mu\text{V/K}$ with a temperature of Ag-substituted Mg_2ZnSb_2 system.

In this case, the VBM was located at the Γ and A points displayed in [Figure 4B](#), indicating a significant improvement in the electrical transport behavior of Mg_3Sb_2 after the substitution of Zn, and Ag into the Mg_2 sites. It also enriches the number of bands in the DOS, which lowers the thermal excitation of the electrons and enables more opportunities for electron transitions, thereby enhancing the electrical transport characteristics in the low-temperature domain and agreeing with experimental results. In addition, [Supplementary Figure 6A-D](#) shows the optimized geometries of Zn at Mg and Sb sites, and Zn-Ag at Mg and Sb sites of Mg_3Sb_2 . The bonding behavior between the foreign dopants (i.e., Zn and Ag) in the Mg_3Sb_2 has been revealed from the PDOS analysis. [Figure 4C](#) and [D](#) shows the VB and CB regions of the energy

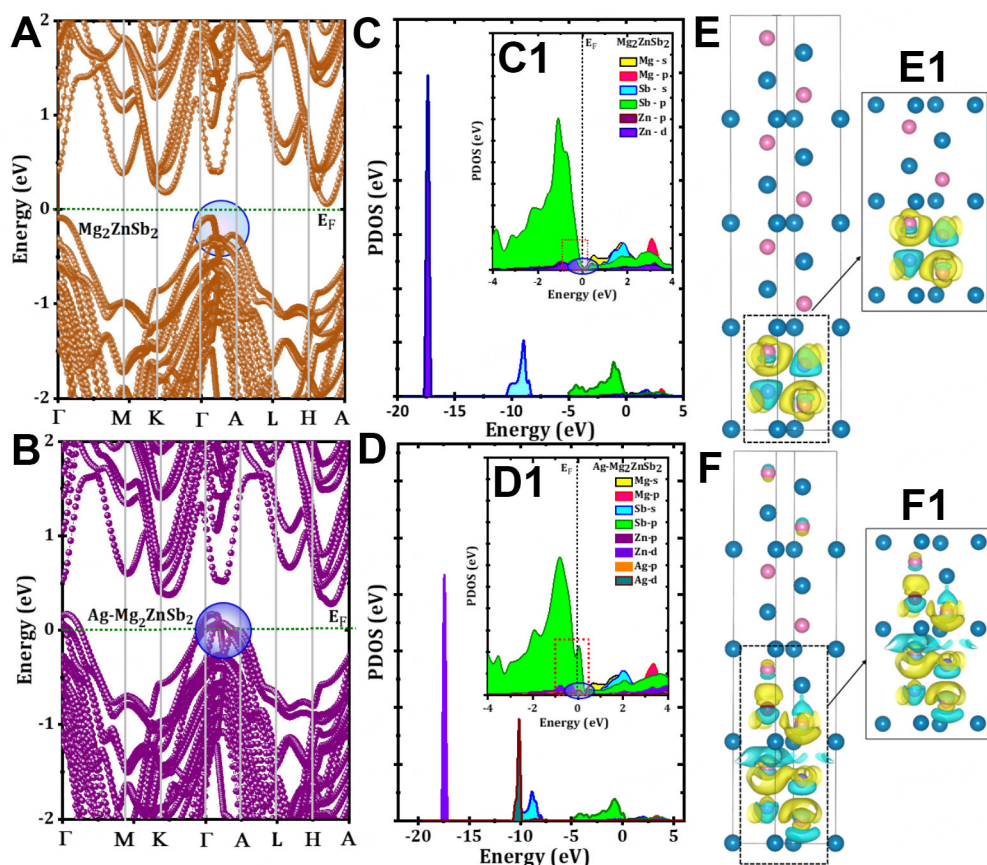


Figure 4. (A and B) The computed band structures; (C and D) PDOS; and (C1 and D1) extracted PDOS (-4 to 4); and (E and F) electron density difference of Mg_2ZnSb_2 and $\text{Ag-Mg}_2\text{ZnSb}_2$ systems. The yellow and red area denotes the loss and gain of electrons. The electron densities of the doped material were taken from $-4.12 \times 10^{-4} \text{ e}/\text{\AA}$. PDOS: Projected density of states.

diagram, which were composed of different orbitals such as Mg-s, Mg-p, Sb-s, and Sb-p, Zn-p, Zn-d, Ag-p, and Ag-d, respectively. Figure 4C1 and D1 represents the extracted PDOS confirming the presence of s, p, d orbitals of Mg, Sb, Zn, and Ag. Additionally, the Mg-p states hybridized with the Sb-s from -0.5 eV to -2.2 eV in the VB region, which clarifies the bonding between Mg and Sb at Mg_3Sb_2 . Supplementary Figure 7A-C shows the TDOS of Mg_2ZnSb_2 and $\text{Ag-Mg}_2\text{ZnSb}_2$. The simulation results agreed with the experimental results, which effectively increased the electron DOS near the E_F . The incorporation of foreign elements into Mg_3Sb_2 is expected to enhance the active sites within the system, thus leading to an improvement in TE performance. Moreover, the electron density difference analysis was used to probe the atomic bonding behavior of Ag with Mg_2ZnSb_2 , as presented in Figure 4E-F1. Furthermore, the electron density difference in Figure 4E1 shows that enhanced electron density is redistributed between Ag/Zn and Mg/Sb atoms of Mg_3Sb_2 , which illustrates that the strong chemical bonding (i.e., Zn-Sb/Mg and Zn-Ag-Sb/Mg) between the dopant elements and the matrix compound, which stabilizes the system. The electron density contour plot in [Figure 4E1 and F1] shows the spherical electron localization between (i) Ag and Sb, (ii) Ag and Mg, and (iii) Zn and Sb elements due to their p and d lone pair interference. These results highlight that the synergistic effect between the foreign and the host material, i.e., Zn-Sb, Zn-Mg, Ag-Sb, and Ag-Mg, could significantly tune the electronic structure and thereby improve the TE properties. Also, it is interesting to note that the substitution of Ag into the Mg_2ZnSb_2 enhances the electron density. The substitution of Ag into the Mg_2ZnSb_2 system increases the active sites of the matrix.

Figure 4E1 shows the Zn-d states, which strongly overlap with Sb-s and Mg-s from -0.2 eV to -1.3 eV of the VB region, implying that Zn-Sb and Zn-Mg bonding structures of Mg_2ZnSb_2 . It is also observed that, the Ag-d orbitals hybridize with the Sb-p and Mg-p near the Fermi and VB regions from -0.21 eV to -0.95 eV, illustrating the Ag-Sb and Ag-Mg bonding states of Ag at Mg_2ZnSb_2 . Furthermore, the Sb-s and Mg-p orbitals hybridize with the Zn-d orbitals from the VB region from ~ -0.51 eV to -1.25 eV indicating the formation of a covalent bond between Zn, Sb, and Mg. Figure 4F1 shows the bottom of the near Fermi region, which is contributed by the intermixing of p-d orbitals of Ag-Sb hybridized bands. This difference in the electronic DOS pattern is responsible for the enhanced m^* due to the incorporation of Ag in the Mg_2ZnSb_2 structure.

Figure 5A represents the PF of undoped and Ag-doped $\text{Mg}_{1.8}\text{Zn}_{1.2}\text{Sb}_2$ samples, which is calculated by $PF = S^2\sigma$. Regardless of the temperature, compared with $\text{Mg}_{1.8}\text{Zn}_{1.2}\text{Sb}_2$, Ag-substituted samples show the increasing trend of PF due to the combination of large S and σ , respectively. When increasing the concentration of Ag ($x = 0, 0.01, 0.03$, and 0.05), the PF value of $167 \mu\text{W}/\text{mK}^2$, $299 \mu\text{W}/\text{mK}^2$, $456 \mu\text{W}/\text{mK}^2$, and $467 \mu\text{W}/\text{mK}^2$ was maximized at 753 K. Specifically, the highest PF observed for $\text{Ag}_{0.05}\text{Mg}_{1.75}\text{Zn}_{1.2}\text{Sb}_2$ of $467 \mu\text{W}/\text{mK}^2$ at 753 K, which is $\sim 180\%$ larger than the $\text{Mg}_{1.8}\text{Zn}_{1.2}\text{Sb}_2$ ($167 \mu\text{W}/\text{mK}^2$). This result confirms that Ag-substitution at Mg sites of $\text{Mg}_{1.8}\text{Zn}_{1.2}\text{Sb}_2$ yields the best control over σ and S to optimize the improved PF at higher temperatures.

Figure 5B represents the μ_w of the as-prepared samples. In addition, the bipolar conduction plays a pivoted role in TE performance at high temperatures, further it can be realized by the μ_w . The μ_w was calculated using measured electrical resistivity and S values by the Drude-Sommerfeld free electron model and analyzed phonon scattering mechanisms, which are calculated by^[66],

$$\mu_w = 331 \frac{\text{cm}^2}{\text{Vs}} \left(\frac{\rho \Omega \text{cm}}{\rho} \right) \left(\frac{T}{300\text{K}} \right)^{-3/2} \left[\frac{\exp \left[\frac{|S|}{k_B/e} - 2 \right]}{1 + \exp \left[-5 \left(\frac{|S|}{k_B/e} - 1 \right) \right]} + \frac{\frac{3}{\pi^2} \frac{|S|}{k_B/e}}{1 + \exp \left[5 \left(\frac{|S|}{k_B/e} - 1 \right) \right]} \right] \quad (5)$$

where $k_B/e = 86.3 \mu\text{V}/\text{K}$, T is an absolute temperature, and ρ is electrical resistivity. This is also a widely used parameter to confirm the scattering mechanisms such as grain boundary scattering at room temperature, ionized impurity scattering ($T^{3/2}$) at room - 450 K, acoustic phonon scattering ($T^{-3/2}$) occurring above 450 K, and so on. Here, compared with undoped $\text{Mg}_{1.8}\text{Zn}_{1.2}\text{Sb}_2$ the μ_w of all the Ag-substituted samples decreases with increasing temperature, which confirms the domination of acoustic phonon scattering ($T^{-0.65}$ to $T^{-1.13}$). Thus, this result helps to correlate with the presence of defects at a concerning temperature. To be specific, the $\text{Mg}_{1.8}\text{Zn}_{1.2}\text{Sb}_2$ and $\text{Ag}_{0.03}\text{Mg}_{1.77}\text{Zn}_{1.2}\text{Sb}_2$ system has strong anharmonicity which is a significant contributor to its low thermal conductivity below $\sim 1 \text{ W}/\text{mK}$. The κ_L of the samples decreases from $\sim 0.73 \text{ W}/\text{mK}$ to $\sim 0.56 \text{ W}/\text{mK}$ for $\text{Mg}_{1.8}\text{Zn}_{1.2}\text{Sb}_2$ and $\text{Ag}_{0.03}\text{Mg}_{1.77}\text{Zn}_{1.2}\text{Sb}_2$ at 753 K, which is $\sim 23\%$ lower than undoped sample. Typically, the independent κ_L served as the key parameter for attaining elevated TE performance through the incorporation of defects in the lattice, offering a novel degree of freedom for modifying the physical parameters to improve the thermal transport properties.

This result confirms that the Ag-substituted $\text{Mg}_{1.8}\text{Zn}_{1.2}\text{Sb}_2$ samples have a lower μ_w value than the undoped $\text{Mg}_{1.8}\text{Zn}_{1.2}\text{Sb}_2$ at room temperature [i.e., 51 to $22.5 \text{ cm}^2/\text{Vs}$]. This is due to the domination of ambient temperature defects such as grain boundaries and ionized impurities. While increasing the measuring temperature, all Ag-substituted samples show higher μ_w values because of microstructural defects such as secondary phases, dislocations, and point defects, respectively. This trend also confirms the domination of acoustic phonon scattering after 453 K. In this, the carrier scattering behavior of the as-prepared samples

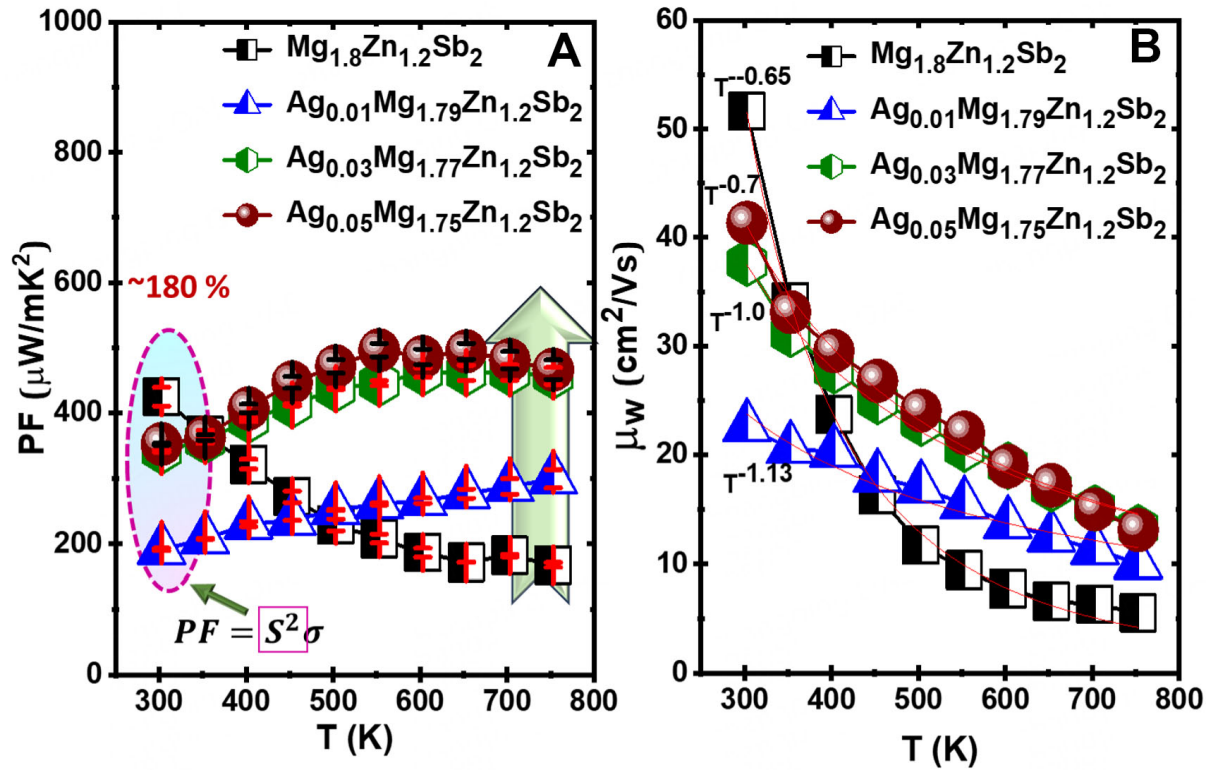


Figure 5. (A) Temperature-dependent power factor (B) weighted mobility of $\text{Ag}_x\text{Mg}_{1.8-x}\text{Zn}_{1.2}\text{Sb}_2$ ($x = 0, 0.01, 0.03$, and 0.05).

was confirmed, and the decreasing trend of μ_w due to the domination of phonon scattering. At 753 K, the μ_w was decreased for all the Ag-substituted samples.

Phonon transport properties and defect analysis

The total thermal conductivity (κ_T) was calculated by $\kappa_T = D\rho C_p$, where D is thermal diffusivity, C_p is specific heat capacity, and ρ is the density of as-prepared pellets. Figure 6A displays the temperature-dependent κ_T of undoped and Ag-substituted $\text{Mg}_{1.8}\text{Zn}_{1.2}\text{Sb}_2$ solid solutions, which obtained the κ_T is less than 1 W/mK. Further, the point defect was introduced via substituting Ag at Mg sites, which helps to reduce the κ_T . However, κ_T increases with Ag content at 303 K, which indicates the domination of electronic thermal conductivity (κ_e) ($\kappa_T = \kappa_L + \kappa_e$). In contrast, the κ_T of Ag-substituted $\text{Mg}_{1.8}\text{Zn}_{1.2}\text{Sb}_2$ samples was reduced at higher temperatures. The lowest κ_T of 0.55 W/mK at 303 K and 0.96 W/mK at 753 K for undoped $\text{Mg}_{1.8}\text{Zn}_{1.2}\text{Sb}_2$. The $\text{Ag}_{0.03}\text{Mg}_{1.77}\text{Zn}_{1.2}\text{Sb}_2$ sample exhibits the κ_T of 0.693 W/mK at 753 K due to increased carrier heat conduction in the lattice, which is 28% lower than the undoped sample. Figure 6B is the κ_e calculated via the Wiedemann-Franz relationship, $\kappa_e = L\sigma T$, where L is the Lorenz number, calculated by a single parabolic band (SPB) model with acoustic phonon scattering assumption. The κ_e increases significantly with the Ag content in the entire temperature range, being consistent with the change of σ . At room temperature, the κ_e of 0.03 W/mK for undoped and 0.12 W/mK for $\text{Ag}_{0.05}\text{Mg}_{1.75}\text{Zn}_{1.2}\text{Sb}_2$ sample, respectively. The undoped $\text{Mg}_{1.8}\text{Zn}_{1.2}\text{Sb}_2$ obtained the κ_e of 0.22 W/mK at 753 K, which is higher than that of Ag-substituted samples.

Figure 6C illustrates the κ_L part of as prepared undoped and Ag-substituted $\text{Mg}_{1.8}\text{Zn}_{1.2}\text{Sb}_2$ samples. The κ_L was calculated by subtraction of κ_e from the measured κ_T ($\kappa_L = \kappa_T - \kappa_e$). In this present investigation, defect engineering was introduced with the substitution of heavy element Ag at lighter Mg sites of $\text{Mg}_{1.8}\text{Zn}_{1.2}\text{Sb}_2$.

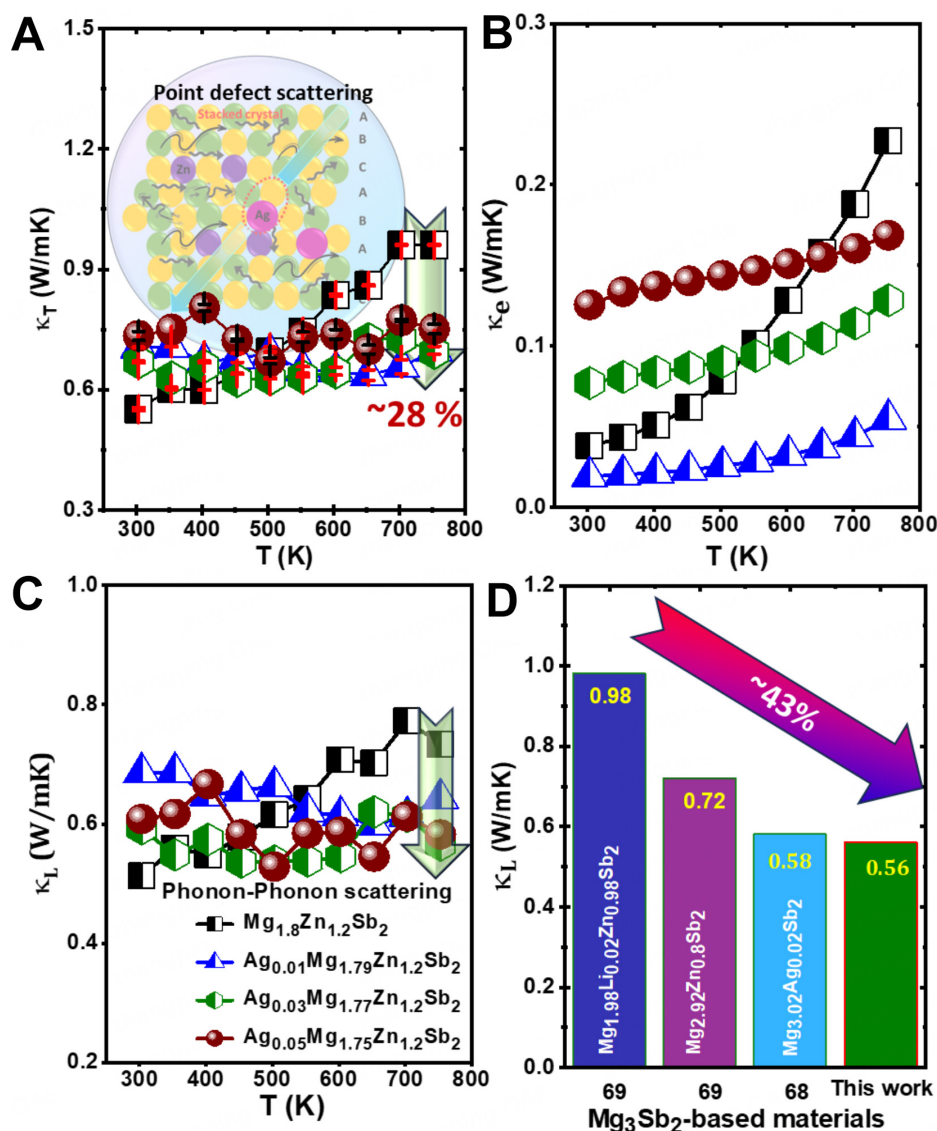


Figure 6. (A-C) Temperature dependence of thermal transport characterization for $\text{Ag}_x\text{Mg}_{1.8-x}\text{Zn}_{1.2}\text{Sb}_2$ (x = 0, 0.01, 0.03 and 0.05), (D) comparison of κ_L with reported work^[68,69].

Based on the formation energy, Ag atoms can replace the tetrahedral $\text{Mg}_2/[\text{Mg}_2\text{Sb}_2]^{2-}$ sites and some excess Ag atoms occupy the interstitial sites of $\text{Mg}_{1.8}\text{Zn}_{1.2}\text{Sb}_2$ system^[45]. Here, the larger atomic radius of Ag is ~165 pm which is lower than Mg (~145 pm), creates mass contraction and enhances the phonon scattering via point defects. This also causes some lattice distortion via the introduction of various wavelengths (short to long) of lattice defects. The charge imbalance between Mg^{2+} and Ag^+ creates the formation of Mg vacancies (produces excess holes), and occupancy of interstitial sites. Therefore, heavier Ag^+ substitution at Mg^{2+} sites creates V_{Mg} and introduces different types of defects such as point defects, dislocation, stacking faults, grain boundaries, and strain in the lattice via atomic dislocations. These defects, identified using HR-TEM, Inverse Fast Fourier Transform (IFFT), and subsequent strain analysis, strengthen the phonon transport properties^[45,67].

The above-mentioned defects promotes the scattering of different wavelength phonons, thus lowering the thermal conductivity of Ag-substituted samples at elevated temperatures. Figure 6D shows the comparison of κ_L with previous reports and present work, which confirms that Ag substitution in the $\text{Mg}_{1.8}\text{Zn}_{1.2}\text{Sb}_2$ solid solution significantly strengthens the various frequency phonon scattering and reduces the κ_L of 0.56 W/mK at 753 K for the $\text{Ag}_{0.03}\text{Mg}_{1.77}\text{Zn}_{1.2}\text{Sb}_2$ sample^[68,69]. Here, it should be noted that the Ag substitution at the Mg site emphasizes the significance of 0D point defects in the lattice via atomic dislocations, which strengthen the phonon transport properties. The high-frequency phonons were scattered via point defects and the relaxation time is $\tau_{PD}^{-1} \sim \omega^4$. In this instance, it can be observed that Mg vacancy and interstitial Ag atoms exhibit a significant capacity to diminish κ_L at similar point defect ratios.

However, the role of the bipolar effect is dominant via ionized impurity scattering which enhances the κ_e at 303 K. Due to the contribution rate of phonon-electron scattering than phonon-phonon scattering, the enhancement of κ_L was obtained at 303 K. After increasing the temperature, the $\text{Ag}_x\text{Mg}_{1.8-x}\text{Zn}_{1.2}\text{Sb}_2$ samples exhibit lower κ_L , which is also the contribution of κ_e .

Further, the microstructure details of $\text{Ag}_{0.03}\text{Mg}_{1.77}\text{Zn}_{1.2}\text{Sb}_2$ sample were investigated by high-resolution TEM characteristics, shown in Figure 7A-F. The intrinsic defects such as grain boundaries (long), dislocations (mid), and stacking faults (short) have been identified using microstructural high-resolution TEM images with Fast Fourier Transform (FFT) and IFFT patterns, respectively. In addition, the lattice strain has been explored via geometric phase analysis (GPA) with HR-TEM results. The mass contraction between Mg and Ag leads to lattice distortion and produces point defects. The existence of stacking faults, which change the atomic arrangement via the scattering of short wavelength phonons and serve as phonon scattering centers via mass and strain fluctuations, was discovered by utilizing the IFFT pattern from the HR-TEM image [Supplementary Table 3]. The heavy element Ag substitution at lighter Mg sites of $\text{Mg}_{1.8}\text{Zn}_{1.2}\text{Sb}_2$ solid solution creates point defects in the form of dislocations and scatter mid-wavelength phonons, respectively^[70]. Further, the different orientations of grains and grain boundaries scatter long wavelength phonons near room temperature. The d-spacing values of 0.26 nm (110), 0.27 nm (110), and 0.35 nm (011) indicate that each grain is crystallized with random orientation shown in Figure 7A. These grain boundaries help scatter the long-wavelength phonons, which are determined by Klemens and Matthiessen's expression $\frac{1}{\tau_{GB}} = \frac{v}{L_G}$, where v is the Poisson ratio and L_G is grain size. Figure 7B represents the IFFT images of dislocation clusters and perfect crystal lattice, which are extracted from Figure 7C. This indicates that Ag substitution introduces different wavelengths of defects and plays a major role in $\text{Mg}_{1.8}\text{Zn}_{1.2}\text{Sb}_2$ solid solution. In Figure 7D and E, the obtained dislocation indicates the heavy Ag substitution in the undoped system leads to changes in the arrangement of atoms, which complicates the atom's interaction and strengthens the phonon scattering [Scheme 1A and B]^[10]. Furthermore, the presence of stacking fault represents Ag substitution interrupting the order of stacked planes in a matrix [Figure 7F]. The obtained defects, such as stacking faults and dislocations, scatter the mid-wavelength phonons and reduce κ_L of the as-prepared samples^[71,72]. Supplementary Figure 8 shows the calculated microstrain vs. κ_L , which confirms the heavy element Ag at anionic Mg2 sites enhances the microstrain significantly scatters the phonons, and reduces the κ_L of as-prepared samples.

In addition, the GPA has been performed to find the interaction of strain and displayed in Figure 7G-H1. Figure 7G and H are the selected strain fields by GPA strain analysis from HRTEM analysis. Figure 7G1-H1 represents the presence of strain clusters and grain boundaries in the axes of ϵ_{xx} and ϵ_{xy} with a scale bar of -1 to 1. The positive value indicates the high magnitude strain in the lattice^[45,73]. This result confirms the influence of Ag in the lattice enhancing high-magnitude lattice strains and strengthening the phonon scattering. Thus, the obtained various defects and lattice strain significantly enhanced the phonon scattering

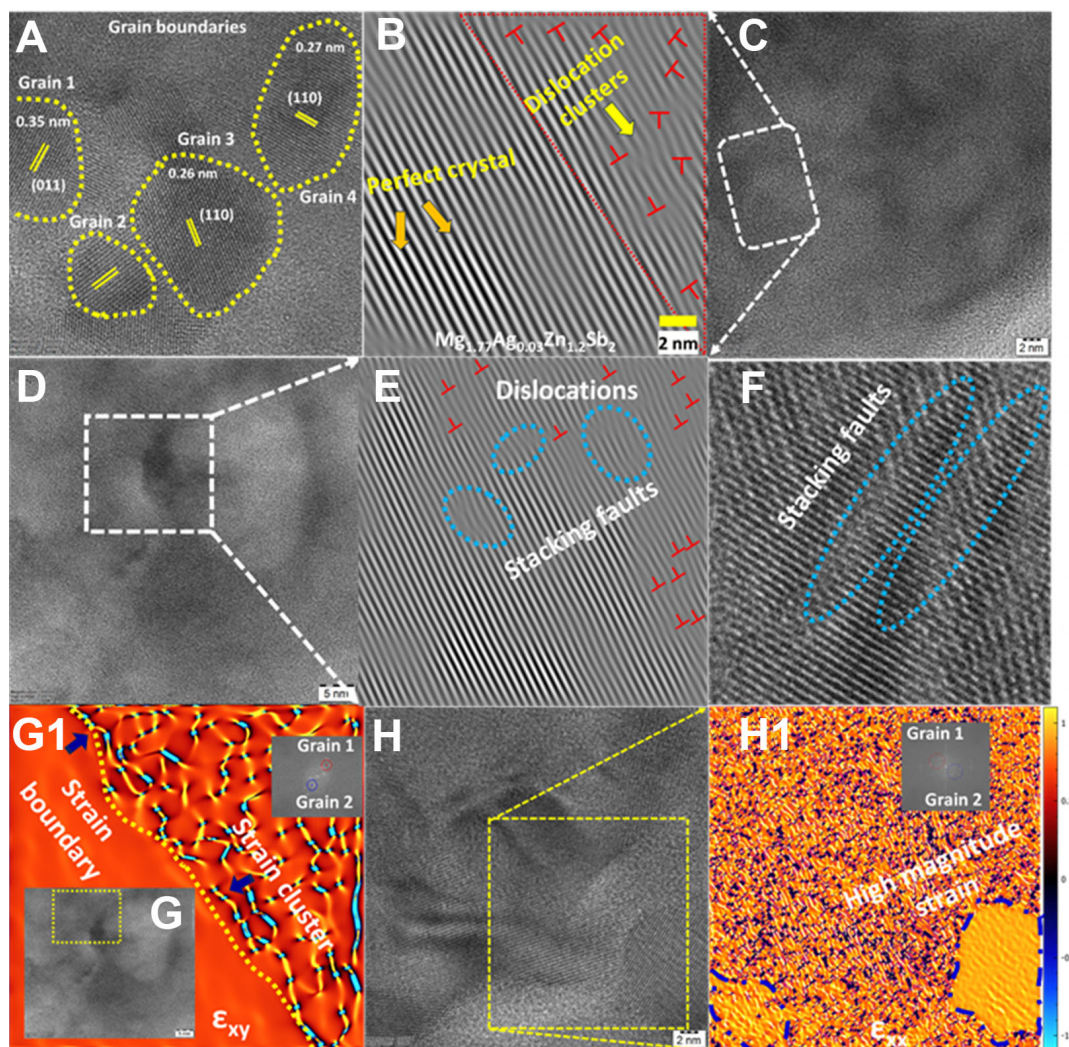
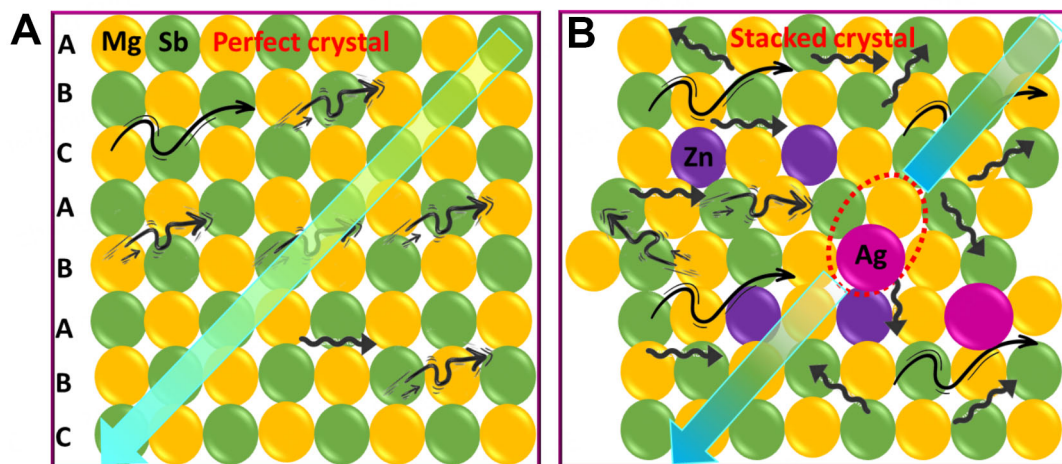


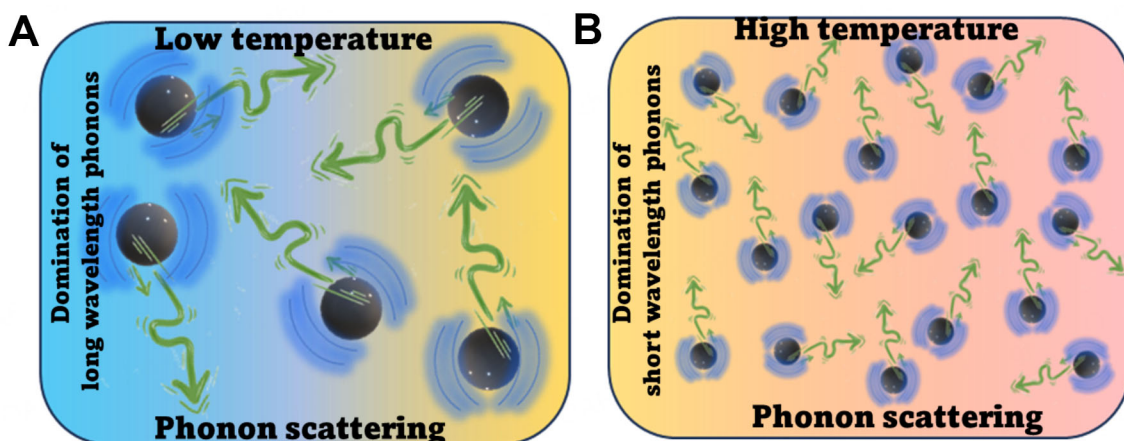
Figure 7. Microstructural and GPA strain analysis of $\text{Ag}_{0.03}\text{Mg}_{1.77}\text{Zn}_{1.2}\text{Sb}_2$ sample: (A) HR-TEM image with grain boundaries; (B) IFFT pattern with dislocations of 7(C); (C) HR-TEM image with dislocations; (D) HR-TEM with defects (E) IFFT pattern of selected portion with dislocations and stacking faults (F) HR-TEM image with stacking faults (G) HR-TEM image with strain (G1) strain distribution (ϵ_{xy}); (H) HR-TEM image with high magnitude strain distribution (H1) high magnitude strain distribution field of 7(H). GPA: Geometric phase analysis; HR-TEM: high-resolution transmission electron microscopy; IFFT: inverse fast fourier transform.

through short to long-wavelength phonons, resulting in lower κ_L of 0.56 W/mK at 753 K for the $\text{Ag}_{0.03}\text{Mg}_{1.77}\text{Zn}_{1.2}\text{Sb}_2$ sample. Scheme 2A and B represents the phonon scattering at a lower and higher temperature range. In general, the long wavelength/low-frequency phonon dominates the scattering at near room temperature range, when temperature increases the wavelength of phonons will decrease and scattering of phonons also increases, which significantly reduces the κ_L of prepared samples.

Figure 8A represents the κ_L comparison graph of $\text{Ag}_x\text{Mg}_{1.8-x}\text{Zn}_{1.2}\text{Sb}_2$ ($x = 0, 0.01, 0.03$, and 0.05) at three different temperature ranges: 303 K, 503 K, and 753 K. From this result, the κ_L value of undoped and Ag-substituted samples gradually decreased with enhancing the doping content and temperature. Figure 8B shows the comparison of PF and zT with Ag content at 753 K. Here, the Ag-substituted $\text{Mg}_{1.8}\text{Zn}_{1.2}\text{Sb}_2$ samples show an enhancing trend with temperature due to the drastic enhancement of the S at high temperatures (at 753 K). Figure 8C shows the temperature-dependent zT of Ag-substituted samples. The



Scheme 1. (A) Phonon scattering in perfect crystal (B) defect structure.



Scheme 2. (A and B) phonon scattering at low and high temperatures.

convergence of multi-band improves the mobility of holes and increases the σ . Therefore, the significant enhancement of S and σ enhances the overall PF and TE performance.

In this investigation, the Ag-substituted Mg_2ZnSb_2 compound exhibits the band convergence of heavy VBs Γ and lighter VB A near E_F of the band structure. Benefiting from the improvement of PF and the significant reduction in κ_L , the Ag-substituted $Mg_{1.8}Zn_{1.2}Sb_2$ samples show considerably increased zT at the entire temperature range. The sample $Ag_{0.03}Mg_{1.77}Zn_{1.2}Sb_2$ shows a peak zT of 0.5 at 753 K, which is $\sim 285\%$ compared to undoped $Mg_{1.8}Zn_{1.2}Sb_2$ ($zT = 0.13$). This suggests that heavy element substitution is an effective strategy for enhancing the TE transport properties of p -type $Mg_{1.8}Zn_{1.2}Sb_2$ -based solid solution. Figure 8D illustrates the comparison graph of a zT values with reported works. This work suggests that the substitution of Ag via multiple scattering strategies leads to synergistic enhancement in the TE performance of Mg_3Sb_3 -based compounds. Compared with reported single and co-doped Mg_3Sb_3 -based compounds, this work achieved the highest zT of ~ 0.5 at 753 K for $Ag_{0.03}Mg_{1.77}Zn_{1.2}Sb_2$. Furthermore, the present work has been compared with previous findings in terms of PF , κ_L , and zT as shown in Supplementary Table 4^[37,45,73–78]. This indicates that Ag substitution at Mg site of $Mg_{1.8}Zn_{1.2}Sb_2$ -based compounds exhibits enhanced carrier and decreased phonon transport properties.

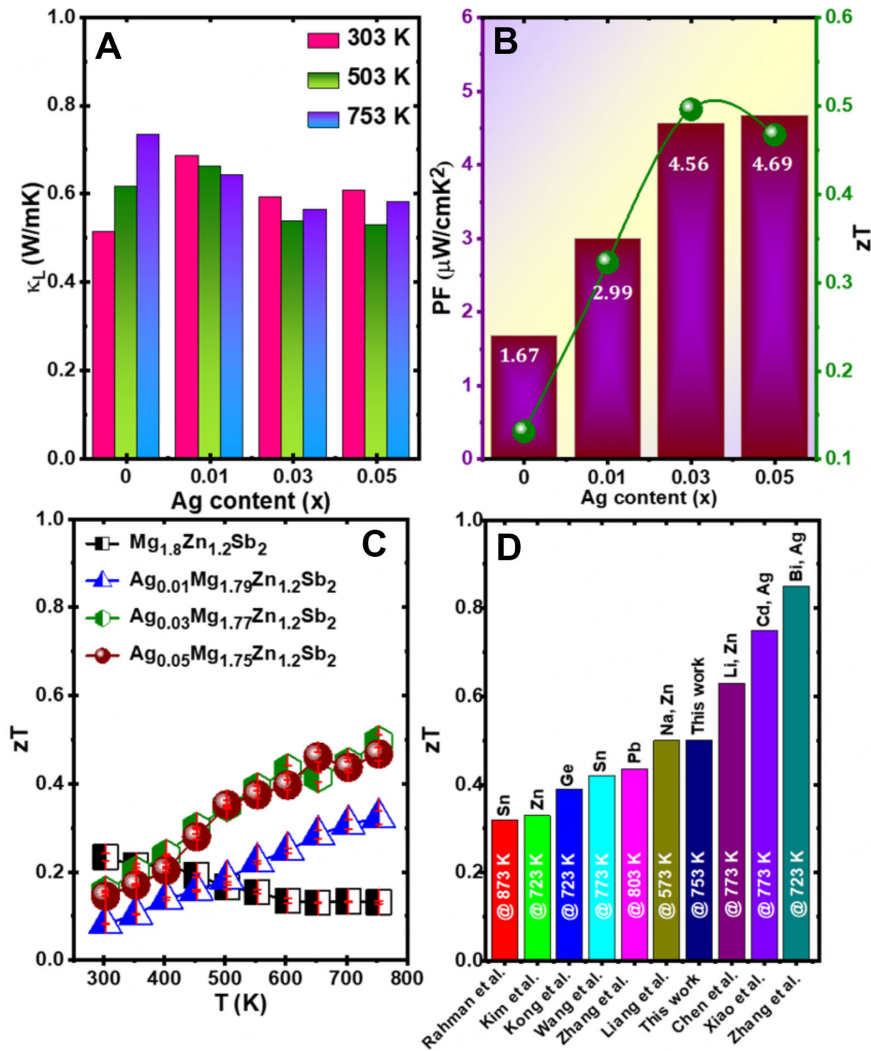


Figure 8. Temperature dependence of (A) κ_l at 303 K, 503 K, and 753 K (B) power factor vs. zT (C) figure of merit of $\text{Ag}_x\text{Mg}_{1.8-x}\text{Zn}_{1.2}\text{Sb}_2$ ($x = 0, 0.01, 0.03$ and 0.05) and (D) zT comparison^[28,36,37,74-77].

Figure 9 represents the TE efficiency (η) vs. zT of $\text{Ag}_{0.03}\text{Mg}_{1.77}\text{Zn}_{1.2}\text{Sb}_2$ sample with temperature difference (303–753 K). The maximum η has been expressed as $\eta = \frac{\Delta T}{T_h} \frac{\sqrt{1+zT} - 1}{\sqrt{1+zT} + T_c/T_h}$. The theoretical η is determined by the calculated zT of the prepared sample and the temperature difference between cold (T_c) and hot sides (T_h). Here, the maximum TE efficiency of 4.9% has been achieved for $\text{Ag}_{0.03}\text{Mg}_{1.77}\text{Zn}_{1.2}\text{Sb}_2$ sample with comparable zT (0.5 K at 753 K).

CONCLUSION

In summary, p -type $\text{Mg}_{1.8}\text{Zn}_{1.2}\text{Sb}_2$ and $\text{Mg}_{1.8-x}\text{Ag}_x\text{Zn}_{1.2}\text{Sb}_2$ ($x = 0.01 - 0.05$) solid solutions have been successfully prepared using spark plasma sintering process and their TE transport properties have been investigated. By Ag substitution on the anion Mg_2 lattice, the n and μ were enhanced, resulting in a VB convergence that leads to narrowed E_g . Thus, the substantially enhanced σ and a noticeably high PF of $456 \mu\text{W/mK}^2$ at 753 K were attained in the Ag substituted samples. Moreover, a greatly suppressed κ_l of 0.56 W/mK at 753 K is also realized due to increased atomic disorder resulting from introduced point defect scattering by Ag, which scatters different wavelengths of phonons. Consequently, remarkable TE performance with a peak zT

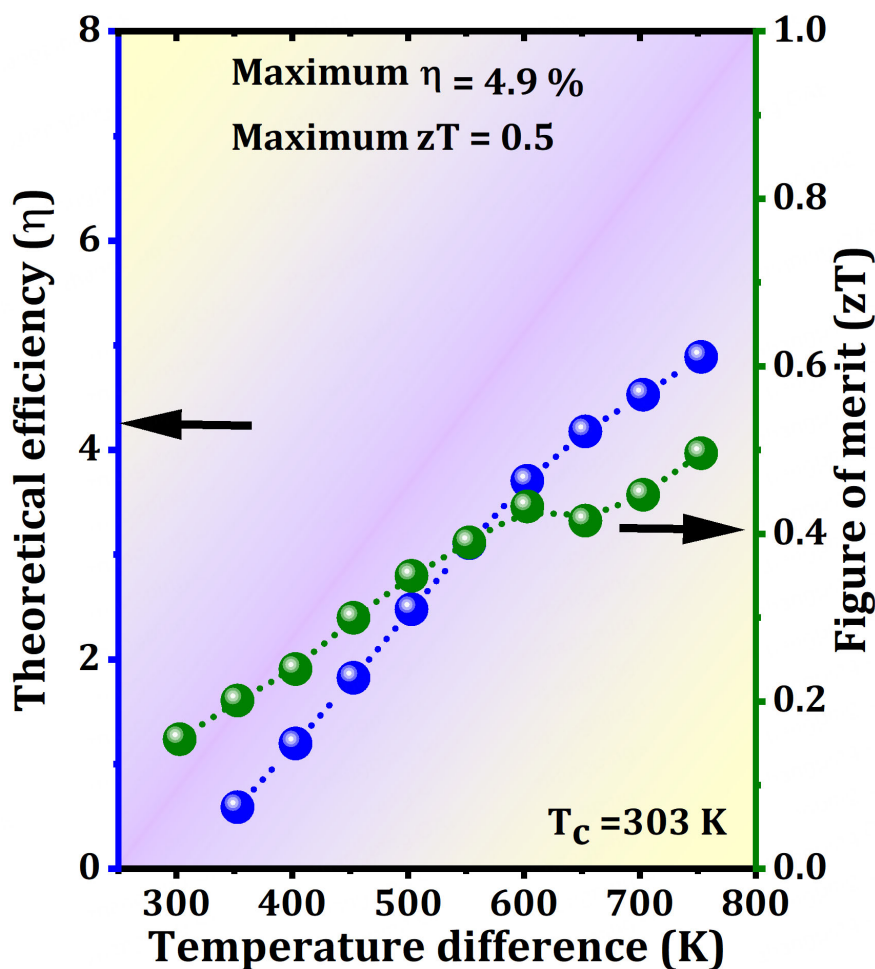


Figure 9. Thermoelectric efficiency vs. zT of $\text{Ag}_{0.03}\text{Mg}_{1.77}\text{Zn}_{1.2}\text{Sb}_2$ sample.

of 0.5 K at 753 K was achieved in the $\text{Ag}_{0.03}\text{Mg}_{1.77}\text{Zn}_{1.2}\text{Sb}_2$ sample. This work thus suggests that heavy aliovalent substitution is an efficient strategy for improving the mid-temperature TE performance of p -type $\text{Mg}_{1.8}\text{Zn}_{1.2}\text{Sb}_2$ solid solutions.

DECLARATIONS

Acknowledgments

The authors acknowledge the Nanotechnology Research Centre (NRC) and Centre of Excellence in Materials for Advanced Technologies (CeMAT) for the experimental and characterization facilities. The authors thank the management of SRM Institute of Science and Technology for the support through the SEED and STARTUP grants.

Authors' contributions

Data sourcing, collection, and analysis, manuscript draft and revision: Shanmugasundaram, P.; Vaiyapuri, V.; Shanmugasundaram, K.; Jayaram, A.

Data sourcing: Shanmugasundaram, P.; Vaiyapuri, V.

Overall supervision, manuscript design and review, funding provision: Ikeda, H.; Mani, N.

Data analysis supervision, manuscript review, revision, and editing: Mani, N.

Availability of data and materials

The data that support the findings of this study are available within the article and its [Supplementary Materials](#).

Financial support and sponsorship

The authors also thank SRMIST for seed and startup grant, DST SERB (CRG/2021/008427), (CRG/2023/000352), CSIR-HRDG (03/1509/23/EMR-II), and DST-FIST [SR/FST/PS-II/2021/190(G)], Government of India, for financial support.

Conflicts of interest

All authors declared that there are no conflicts of interest.

Ethical approval and consent to participate

Not applicable.

Consent for publication

Not applicable.

Copyright

© The Author(s) 2025.

REFERENCES

1. Toberer, E. S.; May, A. F.; Snyder, G. J. Zintl chemistry for designing high efficiency thermoelectric materials. *Chem. Mater.* **2010**, *22*, 624-34. [DOI](#)
2. Eklöf, D.; Fischer, A.; Wu, Y.; Scheidt, E.; Scherer, W.; Häussermann, U. Transport properties of the II-V semiconductor ZnSb. *J. Mater. Chem. A* **2013**, *1*, 1407-14. [DOI](#)
3. Wood, M.; Toriyama, M. Y.; Dugar, S.; et al. Phase boundary mapping of tin-doped ZnSb reveals thermodynamic route to high thermoelectric efficiency. *Adv. Energy. Mater.* **2021**, *11*, 2100181. [DOI](#)
4. Samanta, M.; Ghosh, T.; Chandra, S.; Biswas, K. Layered materials with 2D connectivity for thermoelectric energy conversion. *J. Mater. Chem. A* **2020**, *8*, 12226-61. [DOI](#)
5. Hong, M.; Li, M.; Wang, Y.; Shi, X. L.; Chen, Z. G. Advances in versatile GeTe thermoelectrics from materials to devices. *Adv. Mater.* **2023**, *35*, 2208272. [DOI](#)
6. L.; Beihang University. Carriers: the less, the faster. *Mat. Lab.* **2022**, *1*, 1-3. [DOI](#)
7. Fortulan, R.; Aminorroaya, Y. S. Recent progress in multiphase thermoelectric materials. *Materials* **2021**, *14*, 6059. [DOI](#) [PubMed](#) [PMC](#)
8. Yu, Y.; Zhou, C.; Zhang, S.; et al. Revealing nano-chemistry at lattice defects in thermoelectric materials using atom probe tomography. *Mater. Today* **2020**, *32*, 260-74. [DOI](#)
9. Luo, Z. Z.; Cai, S.; Hao, S.; et al. Strong valence band convergence to enhance thermoelectric performance in pbse with two chemically independent controls. *Angew. Chem. Int. Ed.* **2021**, *60*, 268-73. [DOI](#)
10. Liu, Z.; Mao, J.; Liu, T.; Chen, G.; Ren, Z. Nano-microstructural control of phonon engineering for thermoelectric energy harvesting. *MRS. Bull.* **2018**, *43*, 181-6. [DOI](#)
11. Vijay, V.; Harish, S.; Archana, J.; Navaneethan, M. Cation disorder and bond anharmonicity synergistically boosts the thermoelectric performance of p-type AgSbSe₂. *CrystEngComm* **2021**, *23*, 5522-30. [DOI](#)
12. Kimberly, T. Q.; Ciesielski, K. M.; Qi, X.; Toberer, E. S.; Kauzlarich, S. M. High thermoelectric performance in 2D Sb₂Te₃ and Bi₂Te₃ nanoplate composites enabled by energy carrier filtering and low thermal conductivity. *ACS. Appl. Electron. Mater.* **2024**, *6*, 2816-25. [DOI](#) [PubMed](#) [PMC](#)
13. Heremans, J. P.; Wiendlocha, B.; Chamoire, A. M. Resonant levels in bulk thermoelectric semiconductors. *Energy. Environ. Sci.* **2012**, *5*, 5510-30. [DOI](#)
14. Zhou, M.; Gibbs, Z. M.; Wang, H.; Han, Y.; Li, L.; Snyder, G. J. Thermoelectric performance of co-doped SnTe with resonant levels. *Appl. Phys. Lett.* **2016**, *109*, 042102. [DOI](#)
15. Samanta, M.; Ghosh, T.; Arora, R.; Waghmare, U. V.; Biswas, K. Realization of both n- and p-Type GeTe thermoelectrics: electronic structure modulation by AgBiSe₂ alloying. *J. Am. Chem. Soc.* **2019**, *141*, 19505-12. [DOI](#)
16. Liu, Z.; Zhu, J.; Tong, X.; Niu, S.; Zhao, W. A review of CoSb₃-based skutterudite thermoelectric materials. *J. Adv. Ceram.* **2020**, *9*, 647-73. [DOI](#)

17. Ge, B.; Li, R.; Zhu, M.; Yu, Y.; Zhou, C. Deformation mechanisms of inorganic thermoelectric materials with plasticity. *Adv. Energy. Sustain. Res.* **2024**, *5*, 2300197. DOI
18. Zhang, Y.; Li, Z.; Singh, S.; et al. Defect-engineering-stabilized AgSbTe₂ with high thermoelectric performance. *Adv. Mater.* **2023**, *35*, 2208994. DOI
19. Kihou, K.; Kunioka, H.; Nishiate, H.; Lee, C. Thermoelectric properties of yttrium-doped Mg₃(Sb,Bi)₂ synthesized by melting method. *J. Mater. Res. Technol.* **2021**, *10*, 438-44. DOI
20. Liu, W.; Yin, L.; Li, L.; et al. Grain boundary re-crystallization and sub-nano regions leading to high plateau figure of merit for Bi₂Te₃ nanoflakes. *Energy. Environ. Sci.* **2023**, *16*, 5123-35. DOI
21. Li, X.; Gilbert, J. A.; Trask, S. E.; et al. Investigating ternary Li-Mg-Si Zintl phase formation and evolution for Si anodes in Li-ion batteries with Mg(TFSI)₂ electrolyte additive. *Chem. Mater.* **2021**, *33*, 4960-70. DOI
22. Yuan, Z.; Dahlliah, D.; Hasan, M. R.; et al. Discovery of the Zintl-phosphide BaCd₂P₂ as a long carrier lifetime and stable solar absorber. *Joule* **2024**, *8*, 1412-29. DOI
23. Zhu, Y.; Zhang, W.; Liu, Z.; Li, L. Hydrogen storage properties of the Zintl phase alloy SrAl₂ doped with TiF₃. *J. Alloys. Compd.* **2010**, *492*, 277-81. DOI
24. Brehm, J. A. Predicted bulk photovoltaic effect in hydrogenated Zintl compounds. *J. Mater. Chem. C.* **2018**, *6*, 1470-5. DOI
25. Bhardwaj, A.; Misra, D. K. Enhancing thermoelectric properties of a p-type Mg₃Sb₂-based Zintl phase compound by Pb substitution in the anionic framework. *RSC. Adv.* **2014**, *4*, 34552-60. DOI
26. Zhou, Z.; Han, G.; Lu, X.; Wang, G.; Zhou, X. High-performance magnesium-based thermoelectric materials: progress and challenges. *J. Magnes. Alloys.* **2022**, *10*, 1719-36. DOI
27. Han, Z.; Li, J.; Jiang, F.; et al. Room-temperature thermoelectric materials: challenges and a new paradigm. *J. Materiomics.* **2022**, *8*, 427-36. DOI
28. Xiao, S.; Peng, K.; Zhou, Z.; et al. Realizing Cd and Ag codoping in p-type Mg₃Sb₂ toward high thermoelectric performance. *J. Magnes. Alloys.* **2023**, *11*, 2486-94. DOI
29. Witting, I. T.; Ricci, F.; Chasapis, T. C.; Hautier, G.; Snyder, G. J. The thermoelectric properties of n-type bismuth telluride: bismuth selenide alloys Bi₂Te_{3-x}Se_x. *Research* **2020**, 2020. DOI
30. Xie, S.; Liu, K.; Li, C.; et al. Revealing the temperature-driven Lifshitz transition in p-type Mg₃Sb₂-based thermoelectric materials. *Appl. Phys. Lett.* **2024**, *124*, 093902. DOI
31. Condrón, C. L.; Kauzlarich, S. M.; Gascoin, F.; Snyder, G. J. Thermoelectric properties and microstructure of Mg₃Sb₂. *J. Solid. State. Chem.* **2006**, *179*, 2252-7. DOI
32. Shi, X.; Wang, X.; Li, W.; Pei, Y. Advances in thermoelectric Mg₃Sb₂ and its derivatives. *Small. Methods.* **2018**, *2*, 1800022. DOI
33. Jiang, J.; Zhu, H.; Niu, Y.; et al. Achieving high room-temperature thermoelectric performance in cubic AgCuTe. *J. Mater. Chem. A.* **2020**, *8*, 4790-9. DOI
34. Liu, M.; Guo, M.; Zhu, J.; et al. High-performance CaMg₂Bi₂-based thermoelectric materials driven by lattice softening and orbital alignment via cadmium doping. *Adv. Funct. Mater.* **2024**, *34*, 2316075. DOI
35. Li, J.; Liu, K.; Ma, X.; et al. Improvement of the thermoelectric properties of p-type Mg₃Sb₂ by Mg-site double substitution. *Inorg. Chem.* **2024**, *63*, 20126-32. DOI
36. Zhang, Y.; Liang, J.; Liu, C.; et al. Enhancing thermoelectric performance in P-type Mg₃Sb₂-based Zintls through optimization of band gap structure and nanostructuring. *J. Mater. Sci. Technol.* **2024**, *170*, 25-32. DOI
37. Liang, Z.; Xu, C.; Song, S.; Shi, X.; Ren, W.; Ren, Z. Enhanced thermoelectric performance of p-type Mg₃Sb₂ for reliable and low-cost all-Mg₃Sb₂-based thermoelectric low-grade heat recovery. *Adv. Funct. Mater.* **2023**, *33*, 2210016. DOI
38. Radha, S.; Mani, J.; Rajkumar, R.; Arivanandhan, M.; Jayavel, R.; Anbalagan, G. Effect of Mn and Te doping on thermoelectric transport properties of Mg_{3.2-x}Mn_xSb_{1.97}Te_{0.03} (0 ≤ x ≤ 0.05) Zintl compound: synergistic approach for enhanced thermoelectric performance. *Mater. Sci. Semicond. Process.* **2023**, *165*, 107674. DOI
39. Kannan, V. P.; Lourdhusamy, V.; Paulraj, I.; Liu, C. J.; Madanagurusamy, S. Enhanced thermoelectric performance of p-type Mg_{3-x}Zn_xSb₂/Sb composites: the role of ZnSb/Sb composites. *ACS. Appl. Mater. Interfaces.* **2023**, *15*, 47058-69. DOI
40. Ren, Z.; Shuai, J.; Mao, J.; et al. Significantly enhanced thermoelectric properties of p-type Mg₃Sb₂ via co-doping of Na and Zn. *Acta. Mater.* **2018**, *143*, 265-71. DOI
41. Pack, J. D.; Monkhorst, H. J. "Special points for Brillouin-zone integrations"-a reply. *Phys. Rev. B.* **1977**, *16*, 1748-9. DOI
42. Ohno, S.; Imasato, K.; Anand, S.; et al. Phase boundary mapping to obtain n-type Mg₃Sb₂-based thermoelectrics. *Joule* **2018**, *2*, 141-54. DOI
43. Gong, Y.; Dou, W.; Lu, B.; et al. Divacancy and resonance level enables high thermoelectric performance in n-type SnSe polycrystals. *Nat. Commun.* **2024**, *15*, 4231. DOI
44. Song, L.; Zhang, J.; Iversen, B. B. Thermal stability of p-type Ag-doped Mg₃Sb₂ thermoelectric materials investigated by powder X-ray diffraction. *Phys. Chem. Chem. Phys.* **2019**, *21*, 4295-305. DOI
45. Tiadi, M.; Battabyal, M.; Jain, P. K.; Chauhan, A.; Satapathy, D. K.; Gopalan, R. Enhancing the thermoelectric efficiency in p-type Mg₃Sb₂ via Mg site co-doping. *Sustain. Energy. Fuels.* **2021**, *5*, 4104-14. DOI
46. Sidharth, D.; Srinivasan, B.; Nedunchezian, A. A.; Thirukumaran, P.; Arivanandhan, M.; Jayavel, R. Enhancing the thermoelectric performance of nanostructured ZnSb by heterovalent bismuth substitution. *J. Phys. Chem. Solids.* **2022**, *160*, 110303. DOI
47. Phillips, R.; Jolley, K.; Zhou, Y.; Smith, R. Influence of temperature and point defects on the X-ray diffraction pattern of graphite.

- Carbon. Trends.* **2021**, *5*, 100124. DOI
48. Lei, J.; Wuliji, H.; Ren, Q.; et al. Exceptional thermoelectric performance in AB_2Sb_2 -type Zintl phases through band shaping. *Energy. Environ. Sci.* **2024**, *17*, 1416-25. DOI
 49. Li, J.; Chetty, R.; Liu, Z.; Gao, W.; Mori, T. Enhancing the thermoelectric performance of n-type Mg_3Sb_2 -based materials via Ag doping. *Small* **2025**, *21*, 2408059. DOI
 50. Kim, I.; Jang, K.; Kim, I. Thermoelectric properties of $\text{Mg}_{3-x}\text{Zn}_x\text{Sb}_2$ fabricated by mechanical alloying. *Korean. J. Mater. Res.* **2013**, *23*, 98-103. DOI
 51. Mao, J.; Shuai, J.; Song, S.; et al. Manipulation of ionized impurity scattering for achieving high thermoelectric performance in n-type Mg_3Sb_2 -based materials. *Proc. Natl. Acad. Sci. U. S. A.* **2017**, *114*, 10548-53. DOI
 52. Luo, T.; Kuo, J. J.; Griffith, K. J.; et al. Nb-mediated grain growth and grain-boundary engineering in Mg_3Sb_2 -based thermoelectric materials. *Adv. Funct. Mater.* **2021**, *31*, 2100258. DOI
 53. Chen, X.; Wu, H.; Cui, J.; et al. Extraordinary thermoelectric performance in n-type manganese doped Mg_3Sb_2 Zintl: high band degeneracy, tuned carrier scattering mechanism and hierarchical microstructure. *Nano. Energy.* **2018**, *52*, 246-55. DOI
 54. Song, J.; Luo, P.; Sun, H.; et al. Bismuth-free Mg_3Sb_2 with enhanced room-temperature thermoelectric and mechanical properties. *J. Materiomics.* **2024**, *10*, 1101-8. DOI
 55. Kim, D.; Syers, P.; Butch, N. P.; Paglione, J.; Fuhrer, M. S. Ambipolar surface state thermoelectric power of topological insulator Bi_2Se_3 . *Nano. Lett.* **2014**, *14*, 1701-6. DOI PubMed
 56. Shi, X.; Zhang, X.; Ganose, A.; et al. Compromise between band structure and phonon scattering in efficient n- Mg_3Sb_2 -Bi thermoelectrics. *Mater. Today. Phys.* **2021**, *18*, 100362. DOI
 57. Wei, Z.; Li, Z.; Luo, P.; Zhang, J.; Luo, J. Simultaneously increased carrier concentration and mobility in p-type $\text{Bi}_{0.5}\text{Sb}_{1.5}\text{Te}_3$ through Cd doping. *J. Alloys. Compd.* **2020**, *830*, 154625. DOI
 58. Kumar, R.; Bhatt, R.; Tewary, A.; et al. Synergistic effect of Zn doping on thermoelectric properties to realize a high figure-of-merit and conversion efficiency in $\text{Bi}_{2-x}\text{Zn}_x\text{Te}_3$ based thermoelectric generators. *J. Mater. Chem. C.* **2022**, *10*, 7970-9. DOI
 59. Sarkar, S.; Sarswat, P. K.; Saini, S.; Mele, P.; Free, M. L. Synergistic effect of band convergence and carrier transport on enhancing the thermoelectric performance of Ga doped Cu_2Te at medium temperatures. *Sci. Rep.* **2019**, *9*, 8180. DOI PubMed PMC
 60. Vijay, V.; Karuna, J.; Archana, J.; Navaneethan, M. Phonon-charge carrier dynamics via grain-boundary phase in equilibrium reaction of higher manganese silicide/CNF hybrid composites. *Appl. Phys. Lett.* **2024**, *125*, 171603. DOI
 61. Kannan, V. P.; Lourdhusamy, V.; Paulraj, I.; Madanagurusamy, S.; Liu, C. J. Significantly enhanced thermoelectric performance of p-Type Mg_3Sb_2 via Zn substitution on Mg_2 site: optimization of hole concentration through Ag doping. *ACS. Appl. Mater. Interfaces.* **2024**, *16*, 58677-88. DOI PubMed
 62. Ning, S.; Huang, S.; Zhang, Z.; et al. Band convergence boosted high thermoelectric performance of Zintl compound Mg_3Sb_2 achieved by biaxial strains. *J. Materiomics.* **2022**, *8*, 1086-94. DOI
 63. Ji, Z.; Wei, Z.; Yu, L.; et al. Energy band convergence improves thermoelectric properties of p-type YbMg_2Sb_2 -based materials by solution alloying and biaxial strain. *Appl. Mater. Today.* **2024**, *36*, 102075. DOI
 64. Xia, C.; Cui, J.; Chen, Y. Modulation of band alignment and electron-phonon scattering in Mg_3Sb_2 via pressure. *ACS. Appl. Electron. Mater.* **2020**, *2*, 2745-9. DOI
 65. Xie, S.; Wan, X.; Wu, Y.; et al. Topological electronic transition contributing to improved thermoelectric performance in p-type $\text{Mg}_3\text{Sb}_{2-x}\text{Bi}_x$ solid solutions. *Adv. Mater.* **2024**, *36*, 2400845. DOI
 66. Snyder, G. J.; Snyder, A. H.; Wood, M.; Gurunathan, R.; Snyder, B. H.; Niu, C. Weighted mobility. *Adv. Mater.* **2020**, *32*, 2001537. DOI PubMed
 67. Li, X.; Yang, B.; Xie, H.; et al. Synergistic effects of Mg vacancy and Ag doping on thermoelectric transport properties of p-type Mg_3Sb_2 . *Mater. Res. Bull.* **2023**, *159*, 112106. DOI
 68. Zhang, Q.; Gao, Y.; Xie, H.; Ren, P.; Shan, Z.; Fan, J. Electric wind induced texturing for enhanced thermoelectric performance of p-type Mg_3Sb_2 -based materials. *Appl. Mater. Today.* **2024**, *40*, 102391. DOI
 69. Niu, Y.; Yang, C.; Zhou, T.; et al. Enhanced average thermoelectric figure of merit of p-type Zintl phase Mg_2ZnSb_2 via Zn vacancy tuning and hole doping. *ACS. Appl. Mater. Interfaces.* **2020**, *12*, 37330-7. DOI
 70. Vaiyapuri, V.; Shanmugasundaram, K.; Jayaram, A.; Mani, N. Band flattening and strain field assists an excellent thermoelectric performance of n-type Bi_2Se_3 for room to mid-temperature application. *Small* **2025**, *21*, 2410622. DOI PubMed
 71. Gupta, S.; Ganguli, A. K.; Corbett, J. D. $\text{Mg}_{5.23}\text{Sm}_{0.77}\text{Sb}_4$: an ordered superstructure derived from the Mg_3Sb_2 structure type. *Inorg. Chem.* **2006**, *45*, 8175-8. DOI PubMed
 72. Sootsman, J.; Kong, H.; Uher, C.; et al. Large enhancements in the thermoelectric power factor of bulk PbTe at high temperature by synergistic nanostructuring. *Angew. Chem.* **2008**, *120*, 8746-50. DOI
 73. Priyadharshini, S.; Vijay, V.; Kamalakannan, S.; Archana, J.; Navaneethan, M. Realizing an ultralow thermal conductivity via interfacial scattering and rational-electronic band reformation in p-type Mg_3Sb_2 . *Appl. Phys. Lett.* **2024**, *124*, 031601. DOI
 74. Wang, H.; Chen, J.; Lu, T.; et al. Enhanced thermoelectric performance in p-type Mg_3Sb_2 via lithium doping. *Chin. Phys. B.* **2018**, *27*, 047212. DOI
 75. Kong, D.; Zhao, H.; Fan, X. Enhanced thermoelectric performance of a p-type Mg_3Sb_2 -based Zintl phase compound via Ge doping. *J. Solid. State. Chem.* **2024**, *339*, 124977. DOI
 76. Wang, Y.; Zhang, X.; Liu, Y.; Wang, Y.; Zhang, J.; Yue, M. Optimizing the thermoelectric performance of p-type Mg_3Sb_2 by Sn

- doping. *Vacuum* **2020**, 177, 109388. DOI
77. Rahman, M. M.; Kim, I.; Ur, S. Effect of Sn doping on the thermoelectric properties of P-type Mg_3Sb_2 synthesized by controlled melting, pulverizing followed by vacuum hot pressing. *Korean. J. Mater. Res.* **2022**, 32, 132-8. DOI
78. Prabu, K. V.; Lourdhusamy, V.; Paulraj, I.; Sridharan, M.; Liu, C. Enhancing the thermoelectric power factor of Mg_3Sb_2 with Sn doping on electronegative sites of Sb: effects of reducing the electronegativity difference. *Mater. Chem. Phys.* **2023**, 297, 127379. DOI